

Embedded star clusters and the formation of the Oort Cloud

R. Brassier^{a,b,*}, M.J. Duncan^c, H.F. Levison^d

^a Department of Physics, Engineering Physics and Astronomy, Queen's University, Kingston, ON, Canada

^b Canadian Institute for Theoretical Astrophysics, Toronto, ON, Canada

^c Department of Physics, Engineering Physics and Astronomy, Queen's University, Kingston, ON, Canada

^d SouthWest Research Institute, 1050 Walnut Street, Boulder, CO 80302, USA

Received 6 February 2006; revised 29 March 2006

Available online 5 June 2006

Abstract

Observations suggest most stars originate in clusters embedded in giant molecular clouds [Lada, C.J., Lada, E.A., 2003. *Annu. Rev. Astron. Astrophys.* 41, 57–115]. Our Solar System likely spent 1–5 Myrs in such regions just after it formed. Thus the Oort Cloud (OC) possibly retains evidence of the Sun's early dynamical history and of the stellar and tidal influence of the cluster. Indeed, the newly found objects (90377) Sedna and 2000 CR₁₀₅ may have been put on their present orbits by such processes [Morbidelli, A., Levison, H.F., 2004. *Astron. J.* 128, 2564–2576]. Results are presented here of numerical simulations of the orbital evolution of comets subject to the influence of the Sun, Jupiter and Saturn (with their current masses on orbits appropriate to the period before the Late Heavy Bombardment (LHB) [Tsiganis, K., Gomes, R., Morbidelli, A., Levison, H.F., 2005. *Nature* 435, 459–461]), passing stars and tidal force associated with the gas and stars of an embedded star cluster. The cluster was taken to be a Plummer model with 200–400 stars, with a range of initial central densities. The Sun's orbit was integrated in the cluster potential together with Jupiter and Saturn and the test particles. Stellar encounters were incorporated by directly integrating the effects of stars passing within a sphere centred on the Sun of radius equal to the Plummer radius for low-density clusters and half a Plummer radius for high-density clusters. The gravitational influence of the gas was modeled using the tidal force of the cluster potential. For a given solar orbit, the mean density, $\langle\rho\rangle$, was computed by orbit-averaging the density of material encountered. This parameter proved to be a good measure for predicting the properties of the OC. On average 2–18% of our initial sample of comets end up in the OC after 1–3 Myr. A comet is defined to be part of the OC if it is bound and has $q > 35$ AU. Our models show that the median distance of an object in the OC scales approximately as $\langle\rho\rangle^{-1/2}$ when $\langle\rho\rangle \gtrsim 10 M_{\odot} \text{pc}^{-3}$. Our models easily produce objects on orbits like that of (90377) Sedna [Brown, M.E., Trujillo, C., Rabinowitz, D., 2004. *Astrophys. J.* 617, 645–649] within ~ 1 Myr in cases where the mean density is $10^3 M_{\odot} \text{pc}^{-3}$ or higher; one needs mean densities of order $10^4 M_{\odot} \text{pc}^{-3}$ to create objects like 2000 CR₁₀₅ by this mechanism, which are reasonable (see, e.g., Guthermuth, R.A., Megeath, S.T., Pipher, J.L., Williams, J.P., Allen, L.E., Myers, P.C., Raines, S.N., 2005. *Astrophys. J.* 632, 397–420). Thus the latter object may also be part of the OC. Close stellar passages can stir the primordial Kuiper Belt to sufficiently high eccentricities ($e \gtrsim 0.05$; Kenyon, S.J., Bromley, B.C., 2002. *Astron. J.* 123, 1757–1775) that collisions become destructive. From the simulations performed it is determined that there is a 50% or better chance to stir the primordial Kuiper Belt to eccentricities $e \geq 0.05$ at 50 AU when $\langle\rho\rangle \gtrsim 10^5 M_{\odot} \text{pc}^{-3}$. The orbit of the new object 2003 UB₃₁₃ [Brown, M.E., Trujillo, C.A., Rabinowitz, D.L., 2005. *Astrophys. J.* 635, L97–L100] is only reproduced for mean cluster densities of the order of $10^5 M_{\odot} \text{pc}^{-3}$, but in the simulations it could not come to be on its current orbit by this mechanism without disrupting the formation of bodies in the primordial Kuiper Belt down to 20 AU. It is therefore improbable that the latter object is created by this mechanism.

© 2006 Elsevier Inc. All rights reserved.

Keywords: Comets, dynamics; Orbits; Origin, Solar System; Trans-neptunian objects

1. Introduction and previous work

The reader is referred to Dones et al. (2004) and references therein for a thorough description of previous work on the formation of the Oort Cloud and its dynamics, and to Lada and Lada (2003) for a review of embedded star clusters. For this pa-

* Corresponding author.

E-mail addresses: brasser_astro@yahoo.com (R. Brassier), duncan@astro.queensu.ca (M.J. Duncan), hal@boulder.swri.edu (H.F. Levison).

per, however, those results on which the current work is built are summarized below.

In 1950 Jan Hendrik Oort observed that comets with long periods have their semi-major axes concentrated near $a \sim 10^4$ AU. He therefore proposed that the Sun is surrounded by a spherical cloud of comets whose semi-major axes are of order $a \sim 10^4$ AU (Oort, 1950). In his model, planetary perturbations would have placed the comets on those large, highly eccentric orbits, so that the gravitational perturbations from passing stars can lift their pericentres out of the planetary region. This reservoir of comets is commonly termed the ‘Oort Cloud.’ These same passing stars would occasionally perturb the comets back into the inner Solar System (perihelia $q \lesssim 2$ AU) where they become much more visible due to the formation of cometary tails.

Hills (1981) demonstrated that the phenomenon Oort observed was a selection effect due to the rarity of stellar passages capable of significantly perturbing the pericentres of comets with $a \leq 10^4$ AU. He postulated that the majority of comets could reside in an unseen Inner Oort Cloud (IOC; defined as having $a < 10^4$ AU) at semi-major axes several thousands of AU. The comets with $a > 10^4$ AU are often now called ‘Outer Oort Cloud’ (OOC).

How did the Oort Cloud form: how did the comets end up having such large semi-major axes? An early series of simulations to form the Oort Cloud (OC) were performed by Duncan et al. (1987), henceforth DQT87, in the current Galactic environment with test particles starting on very eccentric orbits with their pericentres in the outer planetary region (4–40 AU). In their model the resulting Oort Cloud has an inner edge at $a \sim 3000$ AU; for $r \in (3000, 50000)$ AU the density of comets decreased quickly with increasing r , and the inclination distribution for the OOC was isotropic. DQT87 demonstrated that, in the current Solar System, comets with initial perihelion $q_0 > 15$ AU and semi-major axis $a_0 \geq 10^3$ AU were much more likely to end up in the OOC than those with smaller pericentres. DQT87 found that there was ~ 5 times more mass in the IOC than in the OOC.

More recently Dones et al. (2004) performed simulations of the formation of the OC in the current Galactic environment. Unlike DQT87, they started the comets on cold orbits between 4 and 40 AU. Contrary to DQT87, they found that the IOC and OOC are about equally massive after 4 Gyr. This discrepancy with the work of DQT87 is caused by the different initial conditions: in the work of DQT87 most of the comets that ended up in the OC did so under the influence of Uranus and Neptune. In the work by Dones et al. (2004), most of the comets ended up under the control of Jupiter (see Fernández, 1997), which only has a 3% efficiency of depositing material in the OC. The total efficiency found by Dones et al. is about 5% at 4 Gyr.

However, Gaidos (1995), Fernández (1997) and Fernández and Bruníni (2000) pointed out that the Sun almost certainly formed in a much denser stellar environment than it is in today. This could result in a much more tightly bound IOC because the denser environment is able to torque the comets away from the planets at a smaller semi-major axis than the current Galactic tide does.

A first attempt to simulate the formation of the OC when the Sun is still in a star cluster was done by Eggers (1999). In that work, the formation of the OC was simulated for 20 Myr using a Monte Carlo method with two star clusters, in which the stellar encounters occurred at constant time intervals and were computed analytically. The first cluster had an effective density of $625 \text{ stars pc}^{-3}$ and the other had an effective density of $6.25 \text{ stars pc}^{-3}$. Both clusters had a velocity dispersion of 1 km s^{-1} . Eggers (1999) defined a comet to be in the OC if $q > 33$ AU and $a > 110$ AU. With these definitions, he obtained efficiencies of 1.7 and 4.8% for the loose and dense clusters, respectively. His model did not include a tidal field caused by the cluster potential. Most objects for the low-density cluster had $a = 6\text{--}7 \times 10^3$ AU and the formed OC was fairly isotropic. For the high-density cluster, most objects were in the range $a = 3\text{--}4 \times 10^3$ AU and again had a fairly isotropic inclination distribution.

Fernández and Bruníni (2000), henceforth FB2K, subsequently performed simulations of the evolution of comets starting on eccentric orbits ($e \sim 0.9$) with semi-major axes 100–300 AU and included an approximate model of the tidal field of the gas and passing stars from the cluster in their model. The cluster had a maximum density of $100 \text{ stars pc}^{-3}$, and the maximal density of the core of the molecular cloud in their models was $5 \times 10^3 M_{\odot} \text{ pc}^{-3}$. Their simulations formed a dense IOC with semi-major axes of a few hundred to a few thousand AU. The outer edge of this cloud was dependent on the density of gas and stars in the cluster. FB2K reported they were able to successfully save material scattered by Jupiter and particularly Saturn, which were the main contributors to forming the IOC, since Uranus and Neptune took too long to scatter material out to large-enough distances (see DQT87). However, as they and others (Gaidos, 1995; Adams and Laughlin, 2001) pointed out, if the Sun remained in this dense environment for long, the passing stars could strip the comets away and portions of the IOC might not be stable.

Very recently, two members of the IOC’s population may have been found: the unusual body (90377) Sedna (Brown et al., 2004) is thought to be a member of the IOC (see, e.g., Morbidelli and Levison, 2004), and perhaps so is the object 2000 CR₁₀₅. The semi-major axes and pericentres of these two objects are $a_s = 501$ AU, $a_{\text{CR}_{105}} = 224$ AU, $q_s = 76$ AU and $q_{\text{CR}_{105}} = 44$ AU. Gladman et al. (2002) proposed that 2000 CR₁₀₅ is part of an Extended Scattered Disk (ESD), using a similar terminology to the Scattered Disk (SD) found by Duncan and Levison (1997). The distinction between the ESD and the IOC is that the former is created by planetary perturbations while the latter requires an external perturber. The ESD is thought to consist of objects with $q > 38$ AU (Gladman et al., 2002) which are thus beyond the gravitational influence of Neptune; objects with smaller q are thought to be part of the SD (Duncan and Levison, 1997), or, to be more precise, a ‘Neptune Scattered Disk.’ Similarly, the IOC contains objects that are no longer under the gravitational influence of Neptune either, and their pericentres are even larger. Gladman et al. (2002) had difficulty in explaining how 2002 CR₁₀₅ obtained $q = 44$ AU apart from needing several Mars-sized objects on orbits far beyond

Neptune, which have been scattered away by now. In this paper, therefore, it is assumed, and subsequently demonstrated, that 2000 CR₁₀₅ can reasonably be placed onto its current orbit by a passing star and hence is a member of the IOC.

A competing model for creating objects like (90377) Sedna, 2000 CR₁₀₅ and 2003 UB₃₁₃ has been investigated by Gomes et al. (2005). In their model, a migrating Neptune traps the comets in mean-motion resonances. Coupled with the Kozai mechanism (Kozai, 1962), these resonances can lift the pericentre to large values and is able to increase the inclination of the object. Gomes et al. (2005) conclude that they cannot produce an object on an orbit similar to that of (90377) Sedna. However, they are able to reproduce 2000 CR₁₀₅. The case of 2003 UB₃₁₃ does not appear to be reproduced either. In their figures, there is one object whose semi-major axis and inclination are similar to 2003 UB₃₁₃, but its pericentre distance is much larger. In those cases where the pericentre and the inclination of an object are similar to those of 2003 UB₃₁₃, the semi-major axis is a lot larger, so that further simulations with better statistics are required to see with what frequency objects on orbits like 2003 UB₃₁₃ might be produced.

The aim of this paper is to investigate the properties of the OC produced by starting with material on initially cold orbits in the Jupiter–Saturn region appropriate to the period before the Late Heavy Bombardment (LHB; Tsiganis et al., 2005) and having them placed in the OC by the combination of perturbations produced by the planets, passing stars and the tidal field of the cluster gas and distant stars. We deliberately have not included the influence of Uranus and Neptune. There are several reasons for doing so. First, the formation processes of Uranus and Neptune tend to be chaotic and erratic and may well take >10 Myr (Thommes et al., 1999). Additionally, Uranus and Neptune take too long to scatter material out to sufficiently large distances that external influences—in this case the gas and stars of the cluster—are able to lift the comets’ pericentres out of the planetary region. This work is an improvement over that of Eggers (1999) because of the model used for the star cluster and the cluster gas and Fernández and Bruníni (2000) because the particles are started on cold orbits.

It is plausible that the ejection of comets from the region of the giant planets happened when gas was present from the primitive solar nebula. At this point the effects of gas drag have not been taken into account, but this is the topic of a forthcoming paper, as is the subsequent evolution of the IOC and OC after the Sun escapes from its birth cluster.

The reader should be made aware that in what follows the term Oort Cloud or OC will be used for both the Inner Oort Cloud and the Outer Oort Cloud for clarity purpose. No distinction shall be made for comets with $a < 10^4$ AU or $a > 10^4$ AU since it is based on the current Galactic Environment and is therefore not applicable to the simulations done during this work. Indeed, it is likely that the distribution we obtain in the OOC will be augmented by the scattering of comets originating in the region beyond Saturn whenever Uranus and Neptune are subsequently formed.

This paper is divided as follows: Section 2 contains a summary of the cluster model that has been adapted. Section 3

contains an analysis of some timescale arguments that arise in the problem. Section 4 consists of the description of the numerical methods and starting conditions used in the simulations. Section 5 contains the results, Section 6 is devoted to conclusions and is followed by Appendices A–C.

2. The embedded cluster

In this section the cluster model is discussed, as are some of the properties of these embedded clusters. Most of the following statements come from Lada and Lada (2003) and the reader is referred to that paper for a more detailed description of these clusters. The adopted model assumes that the Sun formed in an embedded star cluster, which are clusters that are very young and heavily obscured by dust since the molecular gas is still present (Lada and Lada, 2003). The vast majority of the stars that form in these embedded clusters form in rich clusters of 100 or more members with total mass in excess of $50 M_{\odot}$. In fact, most stars probably form in clusters with between 100–1000 members (Adams et al., 2006). Typical populations of embedded clusters within 2 kpc of the Sun today are 50–1500 stars (Lada and Lada, 2003). Therefore, it is assumed that the Sun formed in such a cluster as well. The lifetime of the gas in these clusters is typically 1–5 Myr. Since the formation of unbound stellar clusters is the rule and not the exception (Lada et al., 1984), it is probable that the Sun formed in such a cluster and escaped from it within ≤ 5 Myr. In fact, only 10% of embedded clusters last for 10 Myr (Lada and Lada, 2003).

Recently, Guthermuth et al. (2005) have observed three embedded clusters using near-IR data. The clusters in their sample were chosen because they are rich and relatively young. One of these clusters exhibits clumping of stars into three different regions. The peak volume densities in these clusters in gas and stars are of order 10^4 – $10^5 M_{\odot} \text{pc}^{-3}$, with mean volume densities ranging from 10^2 – $10^3 M_{\odot} \text{pc}^{-3}$. The highest peak volume density quoted is $3 \times 10^5 M_{\odot} \text{pc}^{-3}$. In two of the clusters, their observations show that 72 and 91% of the stars are in locations with stellar densities of $10^4 M_{\odot} \text{pc}^{-3}$ or larger, respectively. For the third cluster this fraction is 24%. These constraints on the stellar density are used in the present work to select a range in central densities of the clusters used.

The reader should note that even though these densities seem very high, one should not interpret this as meaning that there are 10,000–100,000 stars in one cubic parsec. Typically these clusters have 100–1000 members, so the density is just a measure of how compact the cluster is and how close by the stars orbit one another.

For simplicity we adopt a model for the cluster that is often used (e.g., Kroupa et al., 2001) and assume the ratio of stars to gas is constant throughout the cluster. In this so-called Plummer model, the potential $\Phi(r)$ and density $\rho(r)$ are given as a function of distance by (e.g., Binney and Tremaine, 1987)

$$\Phi(r) = \frac{GM}{\sqrt{(r^2 + c^2)}}; \quad \rho(r) = \frac{\rho_0}{(r^2 + c^2)^{5/2}}, \quad (1)$$

where M is the total mass of gas and stars combined in the cluster, r is the distance from the centre of the cluster, c is the

Plummer radius and ρ_0 is the central density of the gas and stars combined. This potential has the properties that the total mass M is

$$M = \int_0^{\infty} 4\pi r^2 \rho(r, c) dr = \frac{4\pi}{3} \rho_0 c^3 \quad (2)$$

and the mass within a radius r of the centre of the cluster is

$$M(r) = \int_0^r 4\pi x^2 \rho(x, c) dx = M \frac{r^3}{(r^2 + c^2)^{3/2}}. \quad (3)$$

The half-mass radius of the cluster can be computed by solving the equation $M(r_{1/2}) = \frac{1}{2}M$ and has the solution

$$r_{1/2} = \frac{\sqrt{3}}{3} (1 + 2^{1/3}) c \approx 1.305 c. \quad (4)$$

Adams et al. (2006) note that observed embedded clusters are often more centrally condensed than Plummer models. However, it will be shown in what follows that the main determinant of the structure of the OC is the mean density the Sun encountered. Thus details of the cluster model are not likely to be important.

The orbit of the Sun in the above potential has a fixed energy and angular momentum so that the pericentric and apocentric distances are constant and the orbit stays in a fixed plane. However, the orbit is non-Keplerian and can best be described as a rosette figure. Fig. 1 shows two solar orbits projected on the x - y plane. The solid line shows the typical rosette figure for a low-eccentricity orbit while the other, shown with a dashed line, is a more radial orbit. The Plummer radius in this figure is about 20,000 AU and the central density is $\rho_0 = 10^5 M_{\odot} \text{pc}^{-3}$.

The effect of the cluster on the dynamics of the comets is as follows: The combined effect of the cluster gas and stars induces a tidal acceleration on the comets. Its derivation and the motion of a comet under the dynamical influence of the Sun and the tidal field is given in Appendix A. In short, the tidal torque induces a coupled oscillation in the eccentricity and the inclination similar to the Kozai mechanism (Kozai, 1962). For inclinations above some critical value, the evolution of the argument of pericentre, ω , is able to change from circulation to libration and the amplitude of variation in eccentricity can increase dramatically. The libration width of ω , as well as the critical inclination above which libration occurs, are a function of $\zeta = c/r_{\odot}$, where r_{\odot} is the distance of the Sun to the cluster centre. As the Sun revolves around in the Plummer potential on an eccentric orbit, the tidal field pulses rhythmically, increasing and decreasing in strength, being maximal near $r_{\odot} \sim c$. The resultant torquing of the comets can lift their pericentre, removing them from the planetary region and stores them temporarily in the OC for a time equal to a precession time (which can be $\gg 1$ Myr). Additionally, the Sun will encounter stars as it orbits the cluster centre. The effect of these passing stars also results in the pericentres of the comets being lifted to large-enough values that they are no longer under the influence of the planets, and thus are safe from being ejected. In addition, the stars can place the comets in regions where the tides do not act, i.e.,

where the precession timescale is long compared to the lifetime of the cluster, so that by the time the Sun leaves said cluster, these comets will stay there.

It is useful to estimate what the timescale is for planetary scattering to move comets to distances where they can be torqued, as well as the time needed to lift their pericentre out of the planetary region. These different timescales will be examined next.

3. Forensic astronomy: Timescale arguments

The evolution of the comets depends on several factors. First, to produce a substantial OC the density of gas and stars averaged over a solar orbit needs to be sufficiently high to lift the pericentres of the comets out of the planetary region in a short enough time to avoid them from being ejected. This can be done by the tides (provided the libration timescale is long compared to the cluster lifetime), stars or both. However, if the density is too high a passing star may strip all the comets away before the Sun leaves the cluster. Second, the density and size of the cluster will determine whether or not there will be any O-stars present (Kroupa et al., 2001). The presence of O-stars is devastating to the interstellar gas (Oort and Spitzer, 1955), which will disappear on the order of a cluster crossing time once an O-star formed (Kroupa, 2000): almost instantaneous compared to the evolution of the cometary orbits in the case of dense clusters.

The O-stars tend to form last (e.g., Henriksen, 1986). The time-delay for the massive stars to form after the smaller ones is thought to be a weak function of the mass. For example, Henriksen (1986) argues that the timescale of formation of a

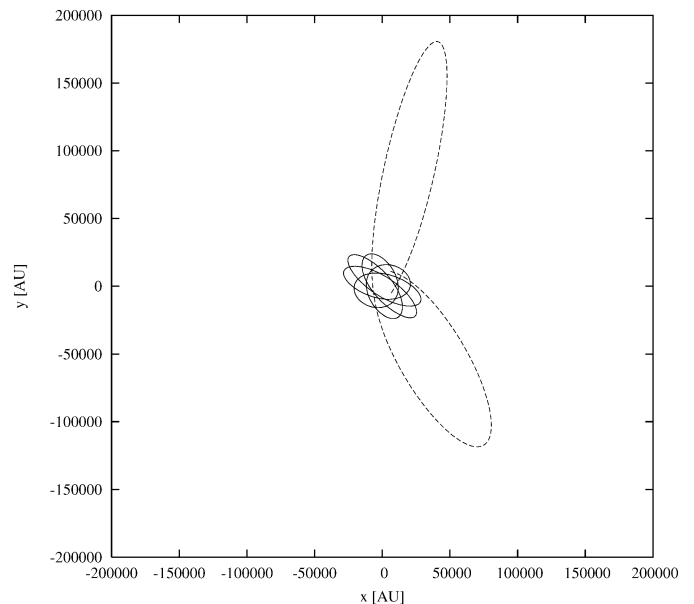


Fig. 1. Two solar orbits for a central density of $\rho_0 = 10^5 M_{\odot} \text{pc}^{-3}$ and a Plummer radius of 20,000 AU projected onto the x - y plane. The solid curve shows the typical rosette figure for a low-eccentricity orbit while the dashed curve shows a highly-eccentric orbit that takes the Sun far from the cluster centre. All units are in AU.

star of mass M_s is

$$t_s = k M_s^{1/4}, \quad (5)$$

where the coefficient $k = 1-3$, the mass M_s is in solar masses and the unit of t_s is in Myr. For an $8 M_\odot$ star the time-delay in formation from that of the Sun is about 1.7–5.4 Myr. However, since the gas lifetime usually does not exceed 5 Myr, the upper limit is not realized. In addition, Bally et al. (1998) found observationally that in the Orion nebula the high-mass stars are younger than those of small mass, supporting the above claim.

Therefore, there might be enough time before the Sun escapes for Jupiter and Saturn to form and scatter comets originally in their vicinity out to sufficiently large distances so that the tides and stars can lift the pericentres of the comets out of the planetary region before they are ejected. Of course, the question remains ‘what is $t = 0$?’ In our model, $t = 0$ corresponds to the moment Jupiter and Saturn have fully formed and begin to significantly scatter material.

For sufficiently large cluster densities, it will be shown that ~ 1 Myr is long enough for the tides to save a fair number of comets before the gas is blown away and the Sun escapes from the cluster. Another issue is the time needed for Jupiter and Saturn to eject the comets versus the time needed by the tides to lift their pericentres out of the planetary region. This will be discussed next.

In Appendix B, the tidal model of DQT87 is adapted to the current situation to derive a formula for the lifting time of the pericentre distance q caused by the cluster tides. It is given by

$$t_q = 1.78 \times 10^{-2} \csc^2 \eta \frac{\Delta q}{\sqrt{q}} \left(\frac{10^3}{a} \right)^2 \left(\frac{10^4}{\rho_0} \right) \frac{(1 + \zeta^2)^{5/2}}{\zeta^3} \text{ Myr}, \quad (6)$$

where a (semi-major axis) and q (pericentre distance) are measured in AU and ρ_0 in $M_\odot \text{ pc}^{-3}$ and η is the comet’s inclination with respect to the plane of the Sun’s orbit about the cluster centre (see Appendix B). It is found to be a good indicator to use the mean density $\langle \rho \rangle$ that the Sun encounters in the cluster, and is typically $\langle \rho \rangle \sim 0.1 \rho_0$ (since $\rho = 0.18 \rho_0$ when $r_\odot = c$ and $\rho = 0.08 \rho_0$ when $r_\odot = r_{1/2}$). The parameter $\zeta = c/r_\odot$ (see Appendix A). As it turns out $\zeta^{-3} (1 + \zeta^2)^{5/2} \sim 10$ for $\zeta \in (0.5, 2)$, which is typical for many orbits, so that one can write

$$t_q \sim 1.78 \times 10^{-2} \csc^2 \eta \frac{\Delta q}{\sqrt{q}} \left(\frac{10^3}{a} \right)^2 \left(\frac{10^4}{\langle \rho \rangle} \right) \text{ Myr}. \quad (7)$$

Another timescale for lifting the pericentres of the comets is the torquing time caused by the perturbations of the passing stars. From DQT87 it is known this has the same functional form as Eq. (6). Hence one has

$$\frac{t_q}{t_*} \approx \frac{3}{4} \csc^2 \eta, \quad (8)$$

where it has been assumed that the mean stellar density is a quarter of the mean gas density because the Stellar Formation Efficiency (SFE; the ratio of gas turned to stars) is taken to be 25%, in accordance with Kroupa et al. (2001). When $\eta = 60^\circ$, which is a typical value, $t_q \approx t_*$, so that from now on only t_q is mentioned. (Of course this argument is invalid when in rare

cases η is very different from 60° or when ζ is either small or large.) These timescales should be compared to the diffusion time, t_d for Jupiter and Saturn to change a comet’s semi-major axis by a factor of two once $a \gg q$, and is given by (DQT87)

$$t_d = 3.16 \sqrt{\frac{10^3}{a}} \left(\frac{10^{-4}}{\sqrt{\langle u^2 \rangle}} \right)^2 \text{ Myr}, \quad (9)$$

where $\sqrt{\langle u^2 \rangle}$ is the rms energy perturbation per perihelion passage. In the pre-LHB system the value of $\sqrt{\langle u^2 \rangle}$ for a given value of q is different than in the current Solar System (see Appendix D), so a plot analogous to DQT87’s Fig. 1 was created and the values of $\sqrt{\langle u^2 \rangle}$ from that graph were used. This result is displayed in Fig. 2. The reader is referred to Appendix D for details of this computation.

Given $\sqrt{\langle u^2 \rangle}$ as a function of q , one can construct the analog of DQT87’s Fig. 2 for the pre-LHB system, once the density of the cluster has been fixed. Fig. 3 shows the values of t_d as a function of a for $q = 5, 7$ and 10 AU (nearly horizontal lines) and lines of t_q for $\Delta q = 5$ AU, $q_0 = 7$ AU, $\eta = 60^\circ$ and $\langle \rho \rangle = 10, 10^3$ and $10^5 M_\odot \text{ pc}^{-3}$ (downward-sloping lines). The line showing the orbital period is also drawn (upward-sloping). Since the quantity $\sqrt{\langle u^2 \rangle}$ is not well defined because of the distribution in u as a function of orbital elements, the value of $\langle |u| \rangle$ was used for the lines showing t_d . The reader is referred to Appendix D for further discussion regarding this issue.

Once the comets are scattered to semi-major axes $a \gg q$, they tend to diffuse outward in semi-major axis along lines of constant q . The comets evolve approximately along the lines of t_d , which are slowly decreasing with increasing a . Two things can happen to the comet, depending on which line it crosses first: if it crosses the period line (increasing with a) before it crosses the line of t_q for a given value of $\langle \rho \rangle$, the comet has a chance of being ejected on the next passage through the region of the jovian planets; if the other case occurs, that is, the line of t_q is crossed before the period line, the comet is usually lifted

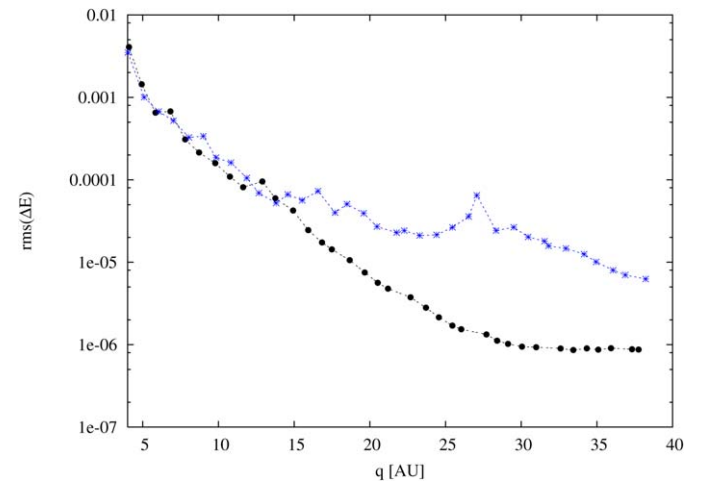


Fig. 2. The rms value of the change in $1/a$ as a function of pericentre distance, q , for the pre-LHB and current Solar System. The pre-LHB data is shown with bullets while the data for the current Solar System is shown with asterisks. There are 36 bins in q containing 270 comets each.

4.2. Cluster parameters and passing stars

The masses of stars were selected using the generating function of Kroupa et al. (1993) with a cutoff at $0.01 M_{\odot}$ instead of $0.08 M_{\odot}$. This was done to make the fit better for low-mass stars while retaining the good fit for heavier stars. The generating function is given by

$$M_j = 0.01 + \frac{0.19\xi^{1.55} + 0.05\xi^{0.6}}{(1 - \xi)^{0.58}}, \quad (10)$$

where M_j is the mass of star j in solar masses and $\xi \in [0, 1)$ is a random number. The distribution of Eq. (10) gives a mean stellar mass of $0.379 M_{\odot}$. For the central cluster density, ρ_0 , we used values 10^2 – $10^6 M_{\odot} \text{pc}^{-3}$ with a star formation efficiency (SFE) of 25%. This value is somewhat on the higher end of the typical range of 5–30% (Lada and Lada, 2003), but in accordance with Kroupa et al. (2001). The upper limit of the central density is chosen because Guthermuth et al. (2005) found a maximum central density of $\rho_0 = 3 \times 10^5 M_{\odot} \text{pc}^{-3}$, so that an upper limit of 10^6 seems justified in the computations.

To generate a catalog of stellar encounters for a given simulation, it was first necessary to construct an N -body realization of the desired Plummer model. Having specified the central density, ρ_0 , and Plummer radius, c , the total cluster mass M (gas plus stars) was then given by Eq. (2). For the assumed SFE and stellar mass function, the number of stars was then 0.66 of the total mass in the cluster. To reproduce the assumed spatial distribution of the stars, each star was assigned an initial radius given by inverting Eq. (3) and consecutively placing each star randomly at a point on a sphere of the prescribed radius. To assign a velocity to each star, it was assumed that the Plummer model had an isotropic velocity distribution, which meant that the phase space volume density followed that of a polytrope of index $n = 5$ (cf. Binney and Tremaine, 1987). This in turn meant that the magnitude v of the velocity vector had a distribution at a given radius r which was proportional to $v^2(\Phi(r) - v^2/2)^{7/2}$, where $\Phi(r)$ is given by Eq. (1). Having specified r for each star, a value of v was drawn from this velocity distribution via a Von Neumann rejection technique (Press et al., 1992). The Cartesian components of the velocity vector were then assigned to assure an isotropic distribution. Finally, the mass of each star was selected using the generating function of Eq. (10).

Having constructed an N -body realization of the desired cluster, the orbits of all stars were integrated using a simple leapfrog integrator under the influence of forces derived from the potential of the gas and distant stars, given in Eq. (1). Close interactions among stars are not incorporated at this stage. For each star with mass in the range 0.8–1.2 solar masses (typically ~ 10 stars in the desired clusters), a catalog of stellar encounter parameters with all the other stars was generated. That is, the time, intruder mass, and position and velocity vectors of each intruder relative to the star in question were recorded when each intruder first encountered a sphere of prescribed radius—typically 0.5–1 Plummer radii. The stellar encounters were later integrated in the RMVS3 simulation described above.

Note that the desire in this paper was to be able to determine the range of OC distributions resulting from a given orbit, i.e., a given stellar eccentricity, inclination and mean distance, in a prescribed cluster. Thus, it was decided to view each star’s orbit as a ‘probe’ of the varying tidal and cluster environment as the star moved on an orbit determined by the overall potential of the cluster. As a result, star–star scatterings, which would cause a given star’s orbit to change unpredictably over several revolutions, were not included in the integration of the orbits since it does not allow for a statistical description of the data. The statistical effects of the individual encounters on the development of the OCs are, of course, incorporated in the SWIFT integrations performed subsequently.

The cluster gas was assumed to be of constant density throughout the runs. This is justified because the gas disappears on the order of a crossing time (Kroupa, 2000) and only after the O-stars form, which appear to form with some delay (Bally et al., 1998).

No binary star encounters were simulated. Even though the majority of stars in the cluster are formed in binaries (e.g., Kroupa, 2000), many of these, especially those widely separated, are disrupted in about twenty crossing times, so that except for the least-dense clusters, most of the wide binaries dissociate within the timeframe of our runs. In some cases the binary nature of the perturbers can be important (Adams and Laughlin, 2001). However, several experiments were performed with parameters appropriate to the clusters used, which showed that binary star encounters with the separations expected in our clusters produced almost identical results to encounters with a single star of the same total mass as the binary system. After our simulations were completed, we became aware of the work of Adams et al. (2006), who found similar results concerning binaries. They performed simulations lasting 10 Myr of embedded clusters for several values of N , the number of cluster members. They argued that many stars have subvirial velocities, i.e., velocities below that set by what is required for the cluster to be in virial equilibrium (see, e.g., André, 2002), which they incorporated in their simulations. Their results show that binary encounters play almost no role in the cluster sizes they examined ($N = 100$ – 1000). Second, from their computed distribution of closest approaches they find that a typical star will have one encounter for the timespan of their simulations in the range $b_c = 700$ – 4000 AU, which is not close enough to appreciably perturb the orbit of the current Neptune. The circumstellar disks are truncated to about 1/3 of this distance (Kobayashi and Ida, 2001), well beyond the current orbit of Neptune, so that most planetary systems survive the birth aggregate without disruption. Third, by performing Monte Carlo simulations of binaries passing by the Sun and the current jovian planets and comparing that to the results of the simulations of their clusters, they show that for clusters containing 300 stars the ejection rate of planets from their stars per cluster of Jupiter-like planets is about 0.15/Myr and 0.7/Myr for Neptune-like planets. Fourth, the authors conclude that in clusters these sizes, FUV radiation does not generally inhibit planet formation. These results are used in our simulations, sometimes implicitly.

A summary of the parameters for each cluster that is used is given in Table 1. The parameter t_c is the crossing time and r_i is the tidal limiting influence of the Sun; it is given in parsec and is computed for $a_\odot = c$. For different values of a_\odot one needs to multiply this by a_\odot/c . Table 2 lists the solar mean distance, eccentricity and inclination with respect to the cluster centre for each run and the mean density averaged over a solar orbit. The mean distance is computed as $a_\odot = (Q_\odot + q_\odot)/2$, where Q_\odot and q_\odot are the apocentre and pericentre of the Sun’s orbit. The eccentricity, although in principle undefined since the orbit is not Keplerian, is computed as $e_\odot = (Q_\odot - q_\odot)/(Q_\odot + q_\odot)$. The latter is basically a means to describe how radial the orbit is, but is not uniquely defined (Adams and Bloch, 2005). The inclination is obtained from the angular momentum vector.

The above method is a significant improvement over that of Eggers (1999). Even though his simulations lasted 20 Myr and ours only 3 Myr, the embedded cluster phase does not usually last longer than about 5 Myr, so that doing the runs for 20 Myr in the embedded cluster environment is unrealistic. In addition, the model employed is self-consistent for both the cluster and the comets, while Eggers (1999) approximated the passing stars from his clusters analytically and used a Monte Carlo method for the comets. Furthermore, the current method is an improvement over that of FB2K since the comets are started on cold orbits in the vicinity of the gas giants.

Table 1
The relevant parameters for the embedded clusters

ρ_0 ($M_\odot \text{ pc}^{-3}$)	c (pc)	σ (km s^{-1})	t_c (Myr)	N	M (M_\odot)	r_i (pc)
10^2	0.8	0.444	1.784	145	214	0.133
10^3	0.4	0.702	0.564	182	268	0.062
10^4	0.2	1.110	0.179	227	335	0.029
10^5	0.1	1.755	0.056	284	419	0.013
10^6	0.05	2.774	0.018	355	524	0.006

The first column lists the central density, the second lists the Plummer radius, the third is the one-dimensional velocity dispersion, the fourth is the crossing time, the fifth is the total number of stars, the sixth is the total mass of the cluster in stars and gas and the last column is the tidal radius of the Sun in pc.

Table 2
The orbital parameters of the solar orbits for each run sorted by run number and central cluster density

Run	10^2	10^3	10^4	10^5	10^6
1	0.437, 0.529, 84.4, 0.599	0.531, 0.622, 80.2, 0.484	1.367, 0.639, 62.8, 0.104	4.853, 0.881, 55.2, 0.01	0.456, 0.473, 27.2, 0.592
2	16060, 0.99995, 100.2, 0.015	1.020, 0.722, 54.3, 0.144	0.904, 0.106, 135.1, 0.224	1.105, 0.578, 116.4, 0.160	0.628, 0.353, 70.0, 0.426
3	0.424, 0.368, 100.8, 0.629	0.590, 0.513, 126.8, 0.449	0.440, 0.649, 122.7, 0.579	0.837, 0.513, 20.2, 0.269	1.438, 0.519, 71.1, 0.086
4	0.546, 0.621, 75.4, 0.445	1.290, 0.465, 72.3, 0.137	0.942, 0.191, 74.3, 0.202	0.730, 0.271, 116.8, 0.341	1.141, 0.095, 37.2, 0.126
5	1.452, 0.317, 110.4, 0.103	1.140, 0.551, 46.8, 0.175	1.328, 0.198, 114.8, 0.080	1.122, 0.438, 55.5, 0.144	1.552, 0.174, 33.6, 0.049
6	1.170, 0.759, 69.9, 0.222	1.013, 0.330, 101.2, 0.186	1.315, 0.352, 99.2, 0.090	1.812, 0.387, 80.8, 0.036	1.414, 0.498, 64.4, 0.087
7	0.762, 0.667, 46.6, 0.355	0.668, 0.834, 15.3, 0.382	1.233, 0.695, 71.3, 0.142	1.265, 0.536, 105.9, 0.117	0.879, 0.895, 95.0, 0.228
8	1.312, 0.706, 79.1, 0.149	0.859, 0.250, 91.1, 0.244	2.345, 0.317, 125.6, 0.013	1.289, 0.499, 42.6, 0.110	1.464, 0.556, 118.8, 0.085
9	2.390, 0.037, 153.6, 0.008	1.500, 0.729, 158.2, 0.088	4.011, 0.640, 95.32, 0.005	2.707, 0.716, 138.7, 0.024	1.624, 0.707, 64.8, 0.079
0	4.258, 0.094, 161.7, 0.001	4.647, 0.490, 77.4, 0.001	9.827, 0.0959, 130.4, 9.06E-6	2.560, 0.632, 45.1, 0.020	3.152, 0.604, 38.7, 0.009

The first entry is the mean distance in parsec, the second is the eccentricity and the third is the inclination, in degrees and the fourth is the mean density of the orbit.

5. Results

In the following section the results of the simulations of the formation of the OC for different cluster central densities, Plummer radii and solar eccentricities and inclinations are presented.

In what follows, three regions of phase space are used to classify objects. At this stage, the primordial ‘Kuiper Belt’ objects are not taken into account. First, the ‘quiescent’ population contains objects with $q < 35$ AU and $e < 0.1$ and is thus bound. The ‘Jupiter–Saturn Scattered Disk’ or ‘JS-SD’ population has $q < 35$ AU and $e > 0.1$ and is bound. Last, a comet is considered part of the OC if it is bound and has $q > 35$ AU. The value of q for OC members is chosen to ensure that the comet will not evolve significantly due to the influence of Neptune, even after the latter has migrated to its current orbit (Fernández et al., 2004). While it might be argued that a threshold value of 40 AU is better, choosing either value does not affect the final outcome significantly: typically <4% of comets in the simulated OC have q between 35 and 40 AU. Only for the highest density clusters does this increase to about 8%. The runs are identified by the central density of the cluster, because this parameter is known beforehand while the average density is not since it depends on the Sun’s orbit. The average density, though, is typically an order of magnitude lower than the central one (see the fourth column of Table 2).

5.1. Overview

For a given cluster density and solar orbits, it can be shown that objects on orbits like that of (90377) Sedna can be reproduced. A sample trajectory is examined to demonstrate how an object ends up on such an orbit (Fig. 4). For this run the central density of the cluster is $\rho_0 = 10^5 M_\odot \text{ pc}^{-3}$ and the Sun’s inclination is $i_\odot = 56^\circ$. Since the Sun’s eccentricity is 0.44, and the mean distance is 1.12 Plummer radii, the orbit-averaged density is computed to be $\langle \rho \rangle = 1.44 \times 10^4 M_\odot \text{ pc}^{-3}$. The comet commences its journey in the vicinity of Jupiter [(a, q) \sim (5, 5)], until it ends up under the influence of Saturn ($q \sim 10$ AU). After rattling around 10 AU, the particle’s semi-major axis, a , gradually increases while its pericentre, q , remains fixed. However, once $a \sim 300$ AU, the cluster tides

lift the particle's pericentre away from Saturn quickly enough to avoid ejection. (From Fig. 3, it can be estimated that for $\langle \rho \rangle \sim 10^4 M_\odot \text{pc}^{-3}$ and $q \sim 10$ AU, this lifting indeed should be likely at $a \sim 200$ AU.) The comet subsequently evolves in q at constant a , which is the reverse of what it does when under the influence of a planet. The particle does not nicely bob up and down in q along lines of constant a because of the influence of the passing stars. The final values at the end of the simulation are $(a, q) = (550, 25)$ AU.

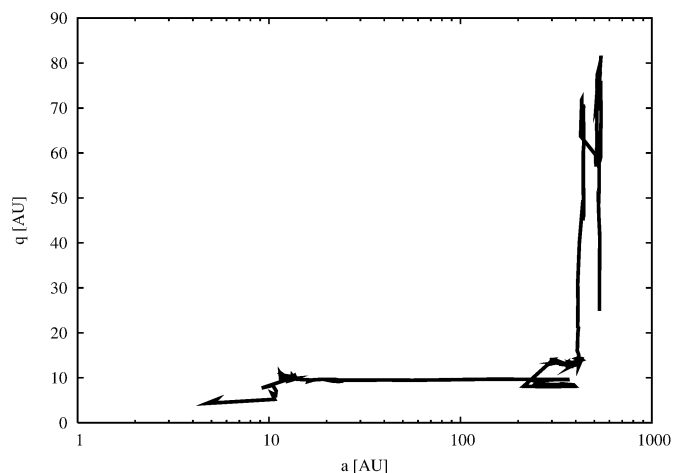


Fig. 4. A sample trajectory in a - q space of a particle that ends up on a Sedna-like orbit. Motion at nearly constant q is caused by planetary perturbations while motion at nearly-constant a is governed by the cluster tide and stars.

Second, the formation of a sample OC as a function of time is examined in the form of a few snapshots. Fig. 5 displays snapshots of the same run as in Fig. 4. The horizontal axis is the instantaneous semi-major axis, a , of the comet while the vertical axis is its instantaneous pericentre distance, q , both measured in the frame centred on the barycentre of the Solar System. Orbits like those of (90377) Sedna, 2000 CR₁₀₅ and 2003 UB₃₁₃ are represented by the big black bullets. The snapshots are taken at 10 kyr, 100 kyr and 1 Myr. Objects with orbits like (90377) Sedna and 2000 CR₁₀₅ are in the resulting OC while there are no objects with orbits like 2003 UB₃₁₃. Additionally, the OC's inner edge is at a smaller semi-major axis than what is predicted with the theory above—this will be discussed in more detail later. Either way, it is clear that the outer edge of the OC is formed first and the inner edge later. This is unsurprising because the comets are torqued faster at larger a than they are closer in. Additionally, infrequent, close passing stars can deposit the comets in the inner region with pericentres large enough and semi-major axes small enough that planet and tidal perturbations act very slowly, thereby shaping the inner regions of the cloud. But what effect does the cluster density have on the location and shape of the OC? This shall again be displayed in the form of a few snapshots.

Fig. 6 shows snapshots at the end of five different runs in a - q phase. The panels show one run selected from each of the different central densities respectively, with the lowest density in the bottom panel and the highest in the top, left one. Objects like (90377) Sedna are typically formed at this time

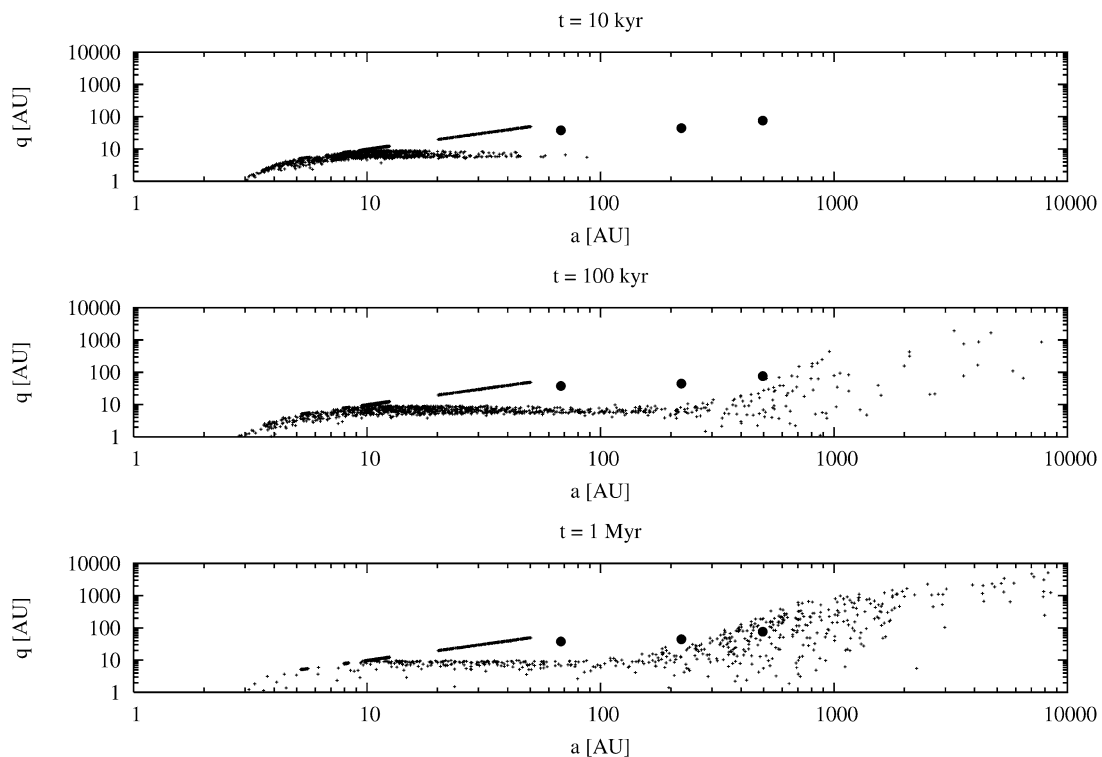


Fig. 5. Snapshots in a - q space at 10 kyr (top panel), 100 kyr (middle panel) and 1 Myr (bottom panel) for one run with $\rho_0 = 10^5 M_\odot \text{pc}^{-3}$. The mean density the Sun encountered during this run is $\langle \rho \rangle = 1.44 \times 10^4 M_\odot \text{pc}^{-3}$. One can see that after 1 Myr (bottom panel) a substantial OC has formed; in this case not much happens after that, so that one ends up with a well-populated OC. The efficiency for this run after 3 Myr is 14%. The positions of (90377) Sedna, 2000 CR₁₀₅ and 2003 UB₃₁₃ are marked with bullets.

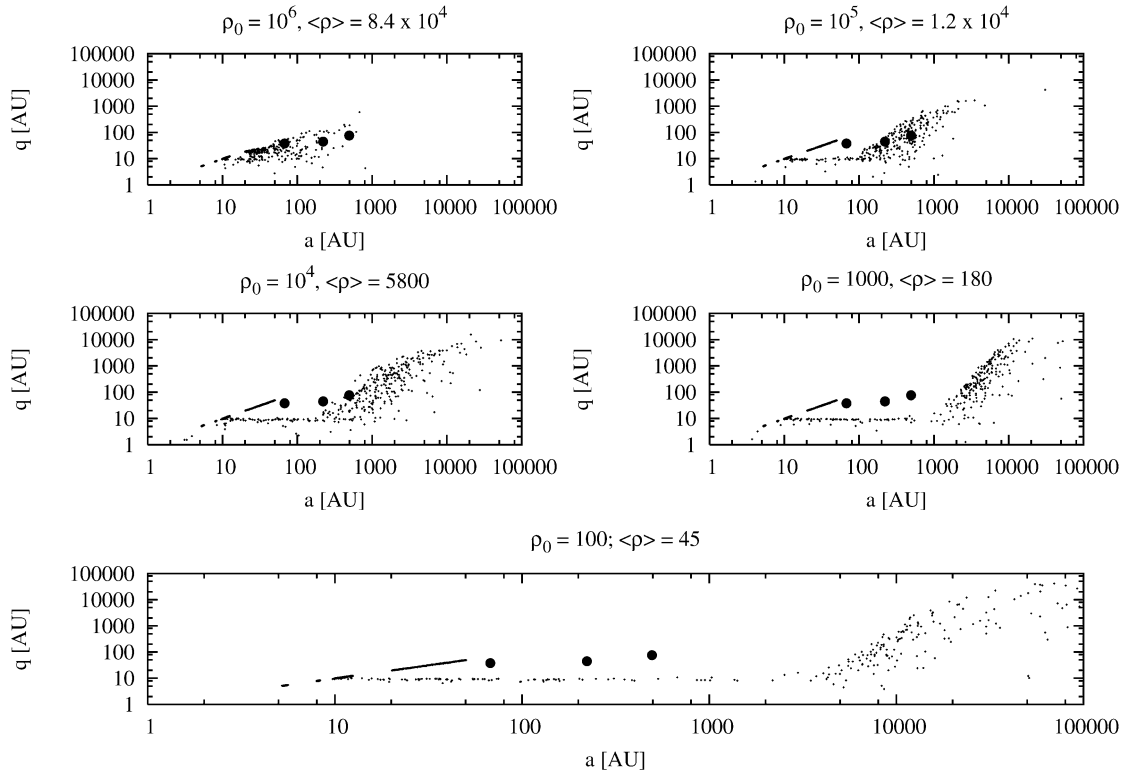


Fig. 6. Snapshots in a - q space at the end of five different runs, one from each set of runs with a different central density. The mean densities the Sun encountered are shown above each panel. The lowest is at the bottom. Note that the extent and median values of a of the members of the OC increase with decreasing density, as is expected. Also notice that objects with orbits like (90377) Sedna and 2000 CR₁₀₅ only form through this mechanism when the density is high.

when $\langle \rho \rangle \gtrsim 10^3 M_{\odot} \text{pc}^{-3}$. This is in good agreement with Fig. 3: for values of a similar to (90377) Sedna, the line for t_d crosses the period line before it crosses the t_q line when $\langle \rho \rangle = 10^3 M_{\odot} \text{pc}^{-3}$ or lower for orbits with $q > 7$ AU, and so the comets are more likely to be ejected rather than saved. The same can be said of 2000 CR₁₀₅ when $\langle \rho \rangle \geq 10^4 M_{\odot} \text{pc}^{-3}$. For higher densities, though, the t_d line crosses the t_q line before it crosses the period line and therefore those comets that do get lifted may have semi-major axes similar to 2000 CR₁₀₅ and (90377) Sedna. This result enables one to narrow down the range in ρ_0 of the cluster from which the Sun originated, provided that the solar eccentricity, inclination and semi-major axis play a lesser role and that (90377) Sedna and 2000 CR₁₀₅ formed through this mechanism. However, it can be seen that an OC can form for all densities. The range in semi-major axis where this cloud resides is a function of the central density: the denser the cluster, the tighter the subsequently formed OC.

Additionally, in the top-left panel, where $\rho_0 = 10^6 M_{\odot} \text{pc}^{-3}$ and $\langle \rho \rangle = 9 \times 10^4$, the stars and tides are stripping away the comets and the location of (90377) Sedna appears close to the outer edge of the formed OC. Even though there are comets beyond its orbit, from the figure one sees the density of dots has decreased significantly. Therefore, providing that the other parameters play a lesser role, the optimum central density at which to form both (90377) Sedna and 2000 CR₁₀₅ within 3 Myr by this mechanism is $\rho_0 = 10^5 M_{\odot} \text{pc}^{-3}$, resulting in an optimal mean density of $\langle \rho \rangle \sim 10^4$; in addition, for this optimal density it turns out that (90377) Sedna is a typical OC member.

5.2. Efficiency

Next it is interesting to know how many of the comets from the Jupiter–Saturn region are in the OC at any time during our simulations. This will once again be demonstrated in the form of a figure.

Fig. 7 displays the fraction of comets in the OC as a function of time for the same runs as Fig. 6, with the densest again being in the top-left panel. Fractions at the end of the runs range from 2–18%, depending on cluster density and time. The fractions of objects in each population are computed as follows: a total of 2200 comets were used per run, 200 of which are in the Kuiper Belt. Since the Kuiper Belt cannot be scattered by Jupiter and Saturn, we do not include them in the statistics used here. This leaves a total of 2000 particles that can be scattered. The “quiescent” population is computed as the number of particles that have $q < 35$ AU and $e < 0.1$ out of the total. This fraction is always 29–30%, caused by Trojans of Jupiter and Saturn as well as a belt of dynamically cold particles beyond Saturn. The only cases where this differs are for a few runs for clusters with $\rho_0 = 10^6 M_{\odot} \text{pc}^{-3}$, in which the planetary system is either destroyed or stirred up by a close stellar passage. Hence 69–70% of particles are dynamically active, i.e., these are part of the non-quiescent population. The fraction of objects in the JS-SD is the fraction of objects out of the *dynamically active* comets that satisfy $q < 35$ AU and $e > 0.1$. For the OC this becomes comets with $q > 35$ AU. During every run, some of the comets end up hitting either Jupiter or Saturn (with a typical ra-

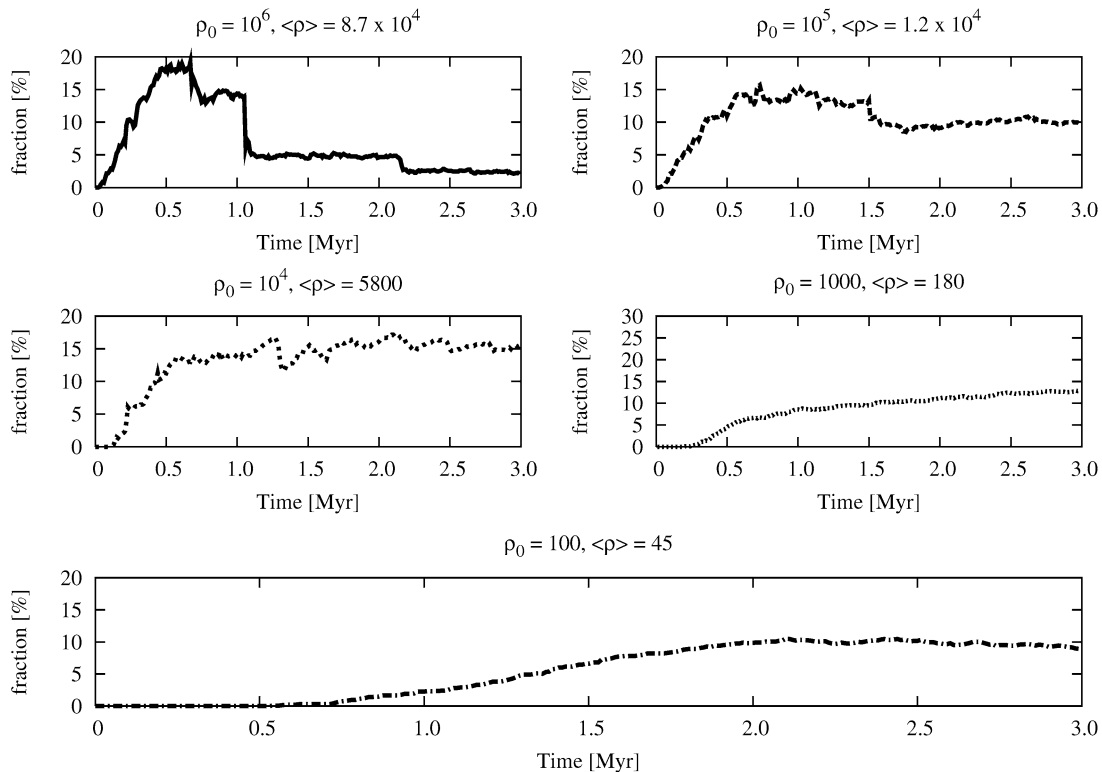


Fig. 7. For the same runs as in Fig. 6, this plot shows the fraction of comets in the OC out of the total number of dynamically active particles still in the simulation. For the low-density clusters the OC takes more time to take shape while for the high-density cases the OC reaches a maximum efficiency well before the end of the run. This decrease is caused by stripping of the comets by the tide and the passing stars.

tio of 3:1 in favor of Jupiter). This fraction of comets hitting a planet is fairly constant for all the runs, and is 7–9% of the dynamically active population. When taken into account, one can compute the fraction of comets that are either too far from the Sun or are ejected (typically 75–85% of the dynamically active population).

One might argue that the fraction of objects in the JS-SD population is not very different from the OC population and thus that our results are not much different from [Dones et al. \(2004\)](#). Yet one has to keep in mind that the JS-SD population continues to evolve after our runs are terminated. The median q for the JS-SD population at the end of most of the runs lies in the vicinity of 9 AU, indicating that, by analogy with the SD simulations of [Duncan and Levison \(1997\)](#), the JS-SD has evolved significantly. However, once Uranus and Neptune have formed and begin to scatter the comets about, the SD population will increase, reach a maximum and then decrease again.

Assuming there are no unusually strong stellar encounters, the efficiency of populating the OC usually reaches a maximum before it falls off again before the end of the runs, although the resulting decrease is slower than the initial building up. The later decrease is caused by three effects: first, distant stellar perturbations either directly strip away the outermost comets or torque the perihelia of some back into the planetary region where ejection may occur; second, some comets end up further than the tidal radius around the Sun, which varies as the Sun orbits the cluster; third, close stellar encounters can change the velocity of the Sun by an amount large enough to leave the

OC unbound ([Levison et al., 2004](#)). These three effects account for the fact that the decrease in efficiency starts later the lower the central density of the cluster, because there are not so many stars to do the stripping and the tidal radius around the Sun is larger as well. This implies that the OC’s population is a function of when the Sun left the cluster. In the top-left panel of Fig. 7, a substantial OC has formed after about 500 kyr. If the Sun were to leave the cluster at that time, the efficiency would be higher than at the end of the run. For high-density clusters is plausible that the Sun left the cluster earlier than for low-density ones, so that the efficiency at 500 kyr is as likely as any other to be representative of the outcome of the simulation and therefore realistic.

5.3. Inclination and argument of pericentre

In this subsection, examples of the distributions in the inclination and the argument of pericentre are given with the help of a few snapshots, to get an idea of the typical orbit of an OC comet.

Fig. 8 depicts the inclination distribution as a function of semi-major axis for the same runs as in Fig. 6. In the middle right panel the distribution is fairly flattened while in the previous three panels the inclination distribution is fairly isotropic. The flattened distribution in the middle right panel is caused by the Sun rushing through the cluster’s pericentre just before the end of the run, which result in a large number of comets getting lifted by a small amount by the tides just before and after the pericentre passage. As can be noted in the top-two

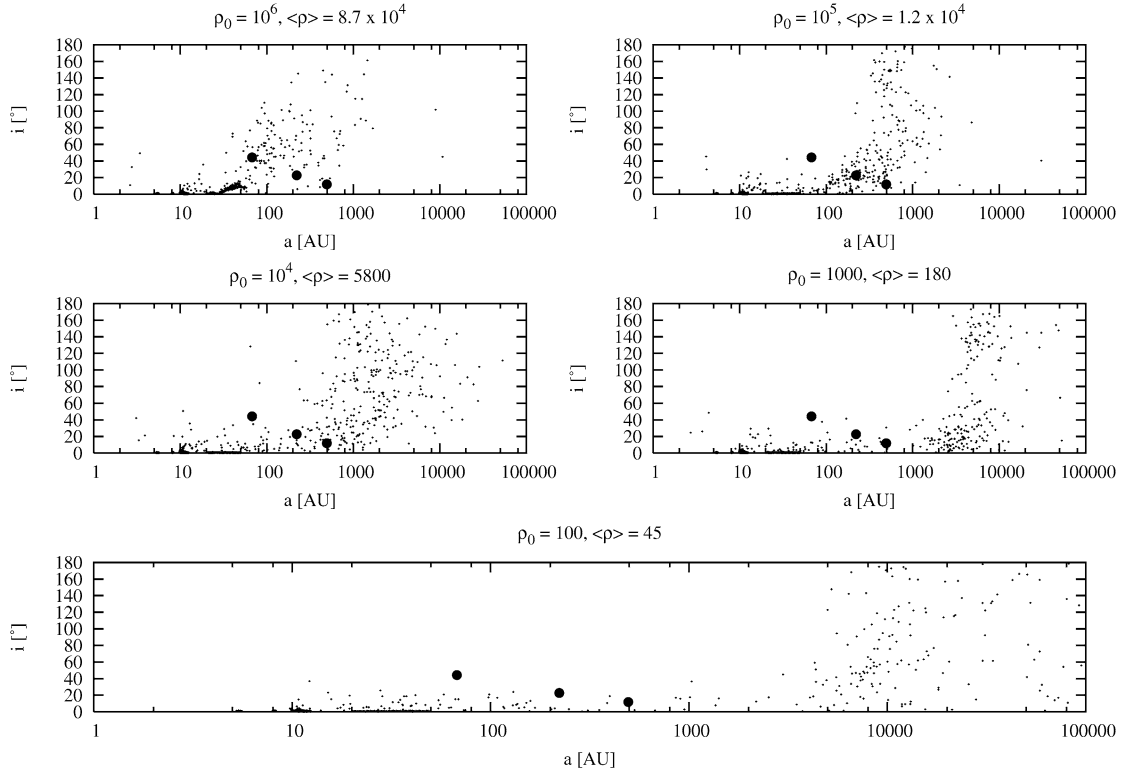


Fig. 8. Snapshots of the inclination distribution as a function of semi-major axis for the same runs as used in Figs. 6 and 7. All panels show significant clustering except the top-left one, suggesting faster evolution and more randomization of orbits.

panels, the distribution beyond a certain value of a , typically those obtained where the values of t_q and t_d for $q \sim 10$ AU intersect, appears isotropic, so that the existence of Sedna-like objects on retrograde orbits is predicted. However, the ratio of prograders to retrograders is determined by $\langle \cos i \rangle$, which usually is close to zero, so that the ratio is about 1:1. One might note that (90377) sedna and 2000 CR₁₀₅ have low-inclination orbits. If the location of 2000 CR₁₀₅ indicates the inner edge of the OC, then the region occupied by (90377) Sedna should contain a significant fraction of objects on retrograde orbits. Further sensitive surveys will be required to determine if this is the case.

The reason some comets are retrograde in the frame of the Solar System is caused by the fact that the angle η , which is the comet's inclination in the cluster frame (see Appendix A), can range from 0° to 90° , due to the Kozai-like mechanism. Initially η is close to i_\odot , which is the fixed inclination of the Solar System plane with respect to the orbit of the Sun. For a prograde solar orbit, although η can only oscillate between two values in the interval 0° – 90° , the inclination of the comet in the Solar System plane, i , can become retrograde. The latter needs to be computed from

$$\cos \eta = \cos i_\odot \cos i + \sin i_\odot \sin i \cos(\Omega - \Omega_\odot), \quad (11)$$

and can reach values larger than 90° , depending on $\Omega - \Omega_\odot$, which is also measured in the Solar System frame. If the coefficient in the second term is larger than the first, then $\cos i < 0$ in order for $\cos \eta > 0$, which can only be satisfied when $i > 90^\circ$.

Now that the inclination distribution is known and can be explained, the distribution in ω is discussed next.

Fig. 9 shows the distribution of ω after 3 Myr. In the top-left panel, the stars randomize the values of ω too quickly in order for the clustering caused by the tides to remain visible at the end of the run. In specific intervals of a , particularly visible in the bottom three panels, the values of ω tend to cluster around 0° and 180° , which is caused by the Kozai effect (see Appendix A). However, it is unlikely that this distribution in ω still exists today for (90377) Sedna-like objects because of precession induced by the planets after the Sun leaves the cluster and, for very distant objects, the Galactic Tide (e.g., Heisler and Tremaine, 1986). To test this hypothesis, we computed the orbit of (90377) Sedna for 4 Gyr under the perturbations of the four jovian planets and the Galactic Tide and found the precession period of ω to be 2.0–2.5 Gyr, allowing for uncertainties in the orbit. An analytical estimate by treating the jovians as an effective J_2 component of the Sun yields $P_\omega = 1.87$ Gyr and $P_\Omega = 3.67$ Gyr (see Appendix C). Comets at (90377) Sedna's location precess on timescales less than or comparable to the age of the Solar System. In addition, the precession is a strong function of inclination and eccentricity, so that the structure seen in Fig. 9 is no longer preserved today because of differential precession. For larger a , the precession time increases.

The figures above gave a qualitative description of the various OCs that were formed during the runs, their locations and distributions in q , i and ω . What follows is a more quantitative description of the same results.

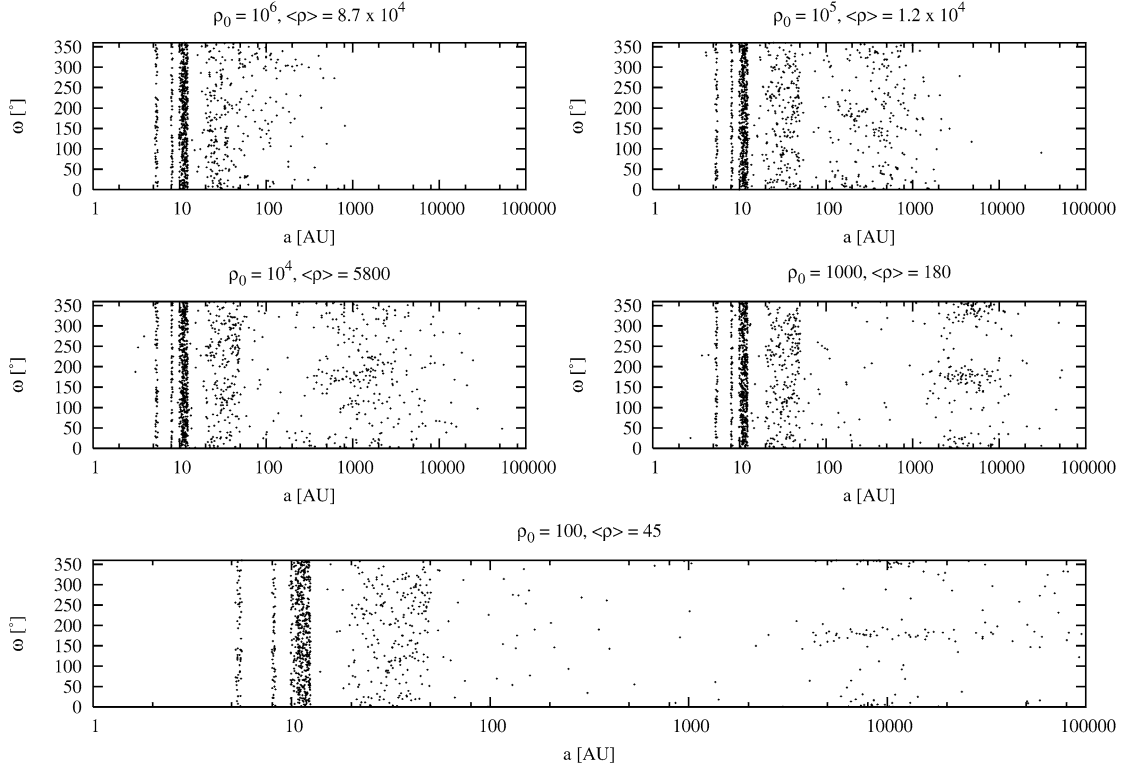


Fig. 9. Snapshots of the distribution of ω as a function of semi-major axis. Significant clustering is apparent, except in the top-left panel, for $\omega = 0^\circ$ and $\omega = 180^\circ$, which is caused by the Kozai-like mechanism induced by the cluster tide. The evolution in ω is slowest around these values (see Appendix A). The values of (90377) Sedna, 2000 CR₁₀₅ and 2003 UB₃₁₃ are not shown since their precession timescales in the current environment are too quick to preserve their original values.

5.4. Statistical analysis

In order to describe the various OCs that were formed during the runs, statistics was performed on the data. In order to correlate the data with the mean density the Sun encountered during the run, this density was computed first and is presented in the fourth column of Table 2.

Since the typical efficiency of placing comets in the OC after 3 Myr is low, there are only a few comets to perform statistics on, resulting in larger errors. Therefore the analysis of the OC was performed over the last 0.5 Myr. Although the runs with the highest density evolve quicker, the averaged results seem to provide a good description. Pooling the data over this time interval resulted in improved statistics.

First, the mean distance of each comet is computed, which is given by

$$\langle r \rangle = \frac{1}{2\pi} \int_0^{2\pi} a(1 - e \cos E) dM = a \left(1 + \frac{1}{2} e^2 \right), \quad (12)$$

where M is the mean anomaly, and subsequently sorted in increasing order. The 10th, 50th and 90th percentile values were then computed and are termed r_{10} , r_{50} and r_{90} . Mean values of e^2 and $\cos i$ were subsequently computed for values of $\langle r \rangle$ centred on r_{10} , r_{50} and r_{90} with a 10% margin on either side, again to allow for better statistics. This data is displayed in Fig. 10. The upper-left panel displays the fraction of dynamically active comets in the JS-SD, the OC and the fraction that is ejected vs

central density. The error bars indicate the minimum and maximum values respectively while the data points are the mean values. The offsets, which are also evident in the next panels, are done for clarity. The next three panels show r_{10} , r_{50} and r_{90} vs ρ_0 in the upper-right panel, the value of $\langle \cos i \rangle$ at r_{10} , r_{50} and r_{90} in the lower-left panel and the value of $\langle e^2 \rangle$ in the lower-right panel. Note that in the lower-left panel, the value of $\langle \cos i \rangle$ at r_{10} is larger than at r_{50} and r_{90} , as expected. In addition, from Fig. 10 one can see that a typical OC member for the runs where $\rho_0 = 10^2 M_\odot \text{pc}^{-3}$ resides much farther away than when, say $\rho_0 = 10^4$. This was shown in Fig. 6. Fig. 11 plots r_{50} vs $\langle \rho \rangle$ and a least-squares fit can be applied when $\langle \rho \rangle > 10$. The slope is $\beta = -0.49 \pm 0.1$. The same slope is obtained when using r_{10} instead of r_{50} and the ratio $r_{50}/r_{10} \approx 3 \pm 1$ for all the runs. The strong correlation between r_{50} and $\langle \rho \rangle$ suggests that the solar inclination does not play a significant role in the extent of the OC but the dominant parameter is mean density (which is determined implicitly by the semi-major axis and eccentricity of the solar orbit). While the strength of the correlation might be surprising, it is no surprise that there is one. After all, the tidal torquing time, t_q , is inversely proportional to $\langle \rho \rangle$, so that in order to lift a comet's pericentre in a short-enough time to prevent ejection by either Jupiter or Saturn, the semi-major axis needs to increase as well to compensate for this slower lifting time.

A natural question to ask is what is the density profile of the OC? Fig. 12 shows $n(\langle r \rangle)$, the density of comets, vs the mean value of the distance, $\langle r \rangle$. The plot shows these profiles for the

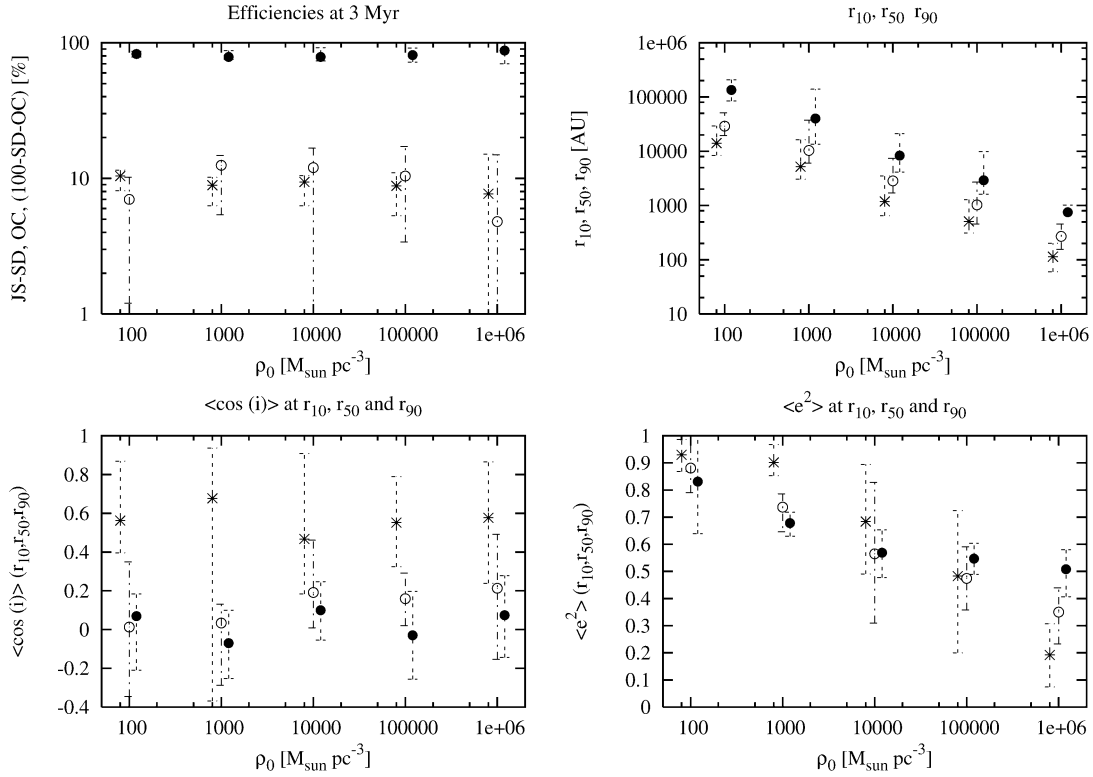


Fig. 10. This plot summarizes the fraction of comets in the JS-SD, the OC and that are ejected in the top-left panel as a function of ρ_0 , the central cluster density. In this panel and the subsequent ones, the error bars denote the minimum and maximum values, while the centre value is the mean over all the runs for that density. Some of the data is offset for clarity. The top-right panel shows the mean values of r_{10} , r_{50} and r_{90} . The bottom-left panel shows $\langle \cos i \rangle$ at r_{10} , r_{50} and r_{90} . The bottom-right panel shows $\langle e^2 \rangle$ at the same distances.

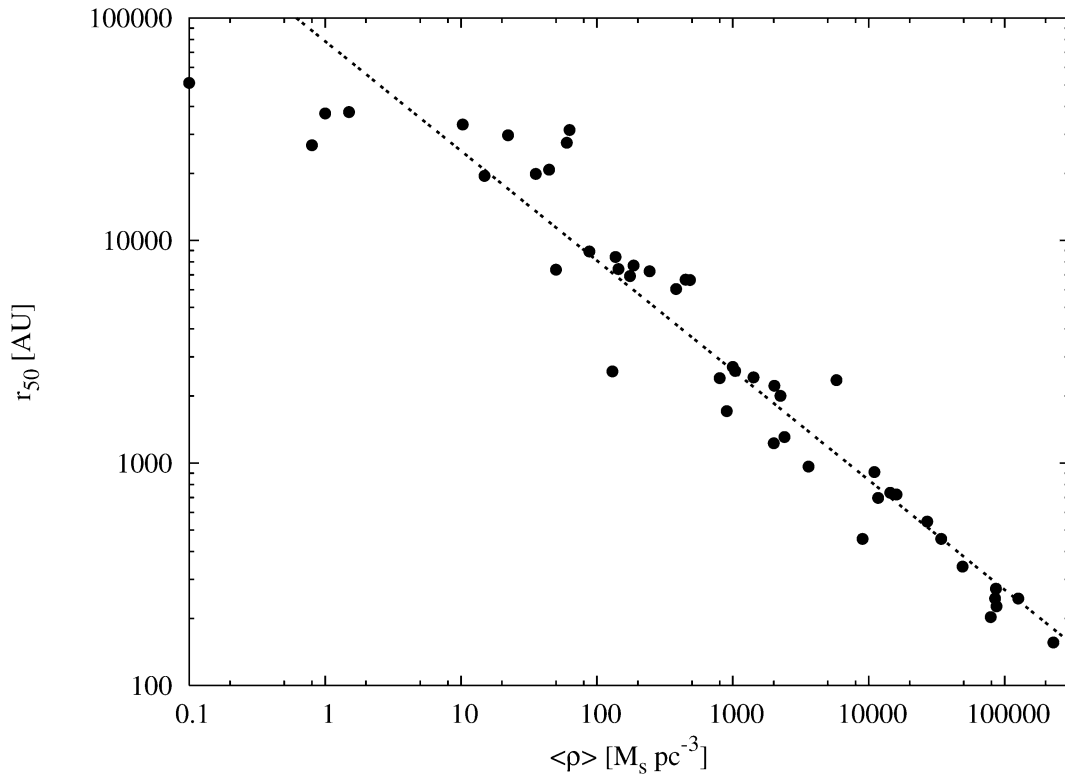


Fig. 11. The median value of an OC comet's mean distance at the end of the runs is plotted vs the mean density the Sun encountered in that particular run. The best-fit curve for $\langle \rho \rangle \gtrsim 10$ is $\langle r \rangle \propto \langle \rho \rangle^{-0.49}$.

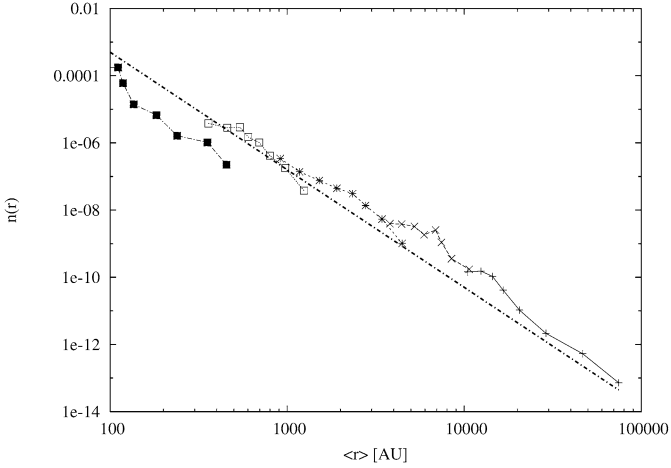


Fig. 12. A plot of the density of comets in the OC, $n(\langle r \rangle)$, as a function of $\langle r \rangle$. The different symbols indicate different clusters and thus different densities. The data is taken from the same runs as in Fig. 6. A least-squares fit gives $n(\langle r \rangle) \propto \langle r \rangle^{-3.5}$, which agrees with DQT87.

same runs depicted in Fig. 6. A least-squares fit to each run separately gives $n(\langle r \rangle) \propto \langle r \rangle^\gamma$, where $\gamma = -3.5$ with an error of about 10%, the same distribution as found by DQT87; it is valid for all the runs and a large range in $\langle r \rangle$, as well as it being valid in the (90377) Sedna region. The straight line in the plot has a slope of -3.5 . Having described the density profiles, the effect of the stars vs the tides in the cluster is examined next.

5.5. Stellar encounters vs tidal lifting

A good description of what happens when a binary system, such as the Sun–comet system, encounters a star is given in Heggie and Hut (1993), who state that physically, high-velocity encounters lead to small changes in the binding energy of the binary, unless the unbound star comes very close to one of the binary components, often destroying the binary in the process.

It has been observed that the most damaging encounters strip away a large portion of the OC: it is the close passages to the Sun that are the most damaging, since they give the Sun a large velocity kick which subsequently unbinds a substantial fraction of the OC (Levison et al., 2004). Slow encounters, on the other hand, are also able to change the binding energy of the Sun–comet binary significantly, provided that the minimum distance of the unbound star is not much greater than the semi-major axis of the binary (Heggie and Hut, 1993). Beyond this distance, the effect of the encounter falls off exponentially.

An issue to be determined in our models is the relative effect of the stars vs the tides. In order not to introduce any bias caused by the solar eccentricity, a total of eight additional runs were performed: two central densities were selected and for each of these, two orbits were chosen: one with a small eccentricity and one with a large one. In half of the runs the stars are included and the tides are set to zero, while in the remaining ones the tides are included and there are no stars. The results were then compared to those runs with both stars and tides present, and are presented in Tables 3 and 4. The differences in Table 3 for r_{10} – r_{90} are not extensive for large densities, indicating that

Table 3

The 10th, 50th and 90th percentile values of the mean distance $\langle r \rangle$ of the OC members for cases with only tides (denoted by ‘T’), only stars (denoted by ‘S’) and both stars and tides (denoted by ‘B’)

Run	10^3	10^5
T1	4196, 6825, 15626	1593, 2870, 8412
S1	4771, 11381, 56768	1029, 2189, 16821
B1	3646, 7275, 27160	1192, 2680, 9812
T2	3487, 6919, 26839	375, 1094, 2226
S2	5533, 10910, 41409	156, 494, 2371
B2	4332, 8225, 25714	170, 447, 2090

Units are in AU. Central cluster densities are on the top.

Table 4

The efficiencies of the same runs from Table 3

Run	10^3	10^5
T1	11.6	24.4
S1	11.1	3.3
B1	13.0	3.4
T2	16.2	8.7
S2	9.7	3.0
B2	12.9	5.9

The units are the same as in Table 3.

in this regime the stars and tides have comparable effects. For the low density this is not the case and the tides clearly dominate. Yet there is one thing that comes to attention: for the low-density runs, the OC formed is more compact and has a smaller value of r_{10} in the case where there are tides only than in the case where there are stars only. This means that, on average, the torquing begins at smaller a when there are tides only. In contrast, the clusters where $\rho_0 = 10^5 M_\odot \text{pc}^{-3}$ show the opposite effect: here the OC formed with stars only has a smaller value of r_{10} though it is almost equally extensive as in the case where there are tides only. This suggests that when the density is high, the cloud is shaped predominantly by stars—especially the inner edge—while for low density it is the tides which do this. In general it is the occasional, close passage of a star that forms the inner edge of the OC.

Fig. 13 shows the efficiency vs time for one of the runs with $\rho_0 = 10^5$ and $\langle \rho \rangle = 1.44 \times 10^4$. In the case with tides only (top panel) the number of comets in the OC increases smoothly. One might ask whether or not the comets return after a libration timescale. This does seem to happen on occasion, but even distant comets have libration timescales of order a million years, so that they may not even return before the simulation is stopped, since it also takes time for the comets to get to the OC as well. In the case with stars only (middle panel), the process is stochastic, as expected. The bottom panel is more or less a smoothed version of the middle one. One can see that in the case where the stars are present, the efficiency reaches a maximum and then decreases before the end of the run is reached. This is probably caused by the stars stripping the comets and the reduction in the number of comets left in the scattered disk to replenish the lost OC. Also notice that, for the runs with a high density, the efficiency in the cases where stars are present is much less than in the case where there are only tides. This implies that while the stellar encounters are capable of lifting a fraction of comets into the OC, they are even more capable of stripping

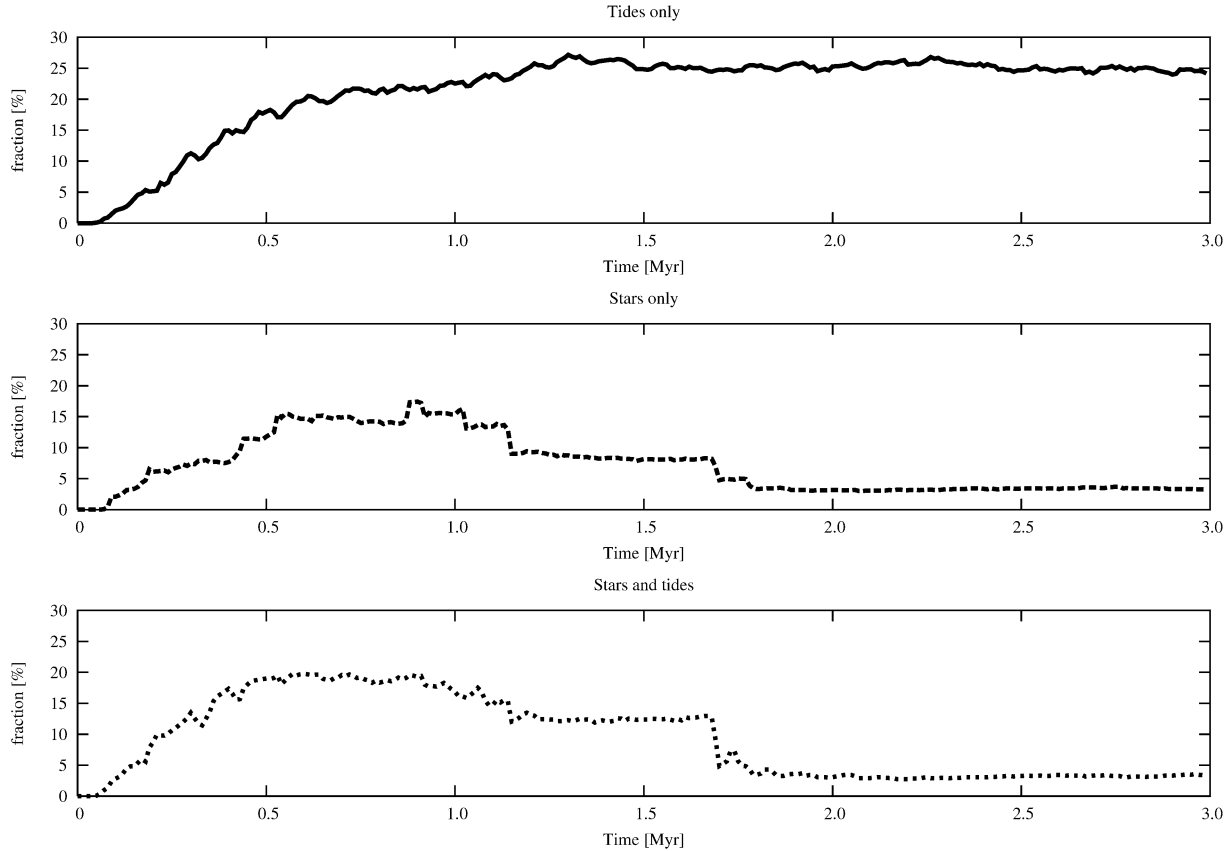


Fig. 13. Plots of the fraction of comets that are in the OC out of the total number of comets still in the run, for a case with tides only (top panel), stars only (middle panel) and both tides and stars (bottom panel). The mean density of the cluster with both tides and stars is $\langle\rho\rangle = 1.44 \times 10^4 M_{\odot} \text{pc}^{-3}$. Note that the formation of the OC happens smoothly in the case where there are tides only, while in the cases where stars are present the process is much more stochastic, as is expected. Also notice that the stars are quite damaging to the OC in this case.

away these same comets through different encounters. The efficiencies of each run are shown in Table 4: for the runs with low density, the efficiencies for both stars and tides are similar, while for the high-density runs the efficiency using tides only is much larger than with the stars present. This reaffirms that in an environment with high density, the stars play a relatively larger role than in a low-density environment and are more destructive. It should be noted that stars and tides can act very differently for a small set of particular orbits, e.g., for the Sun on a nearly-circular orbit deep inside the core of the cluster. However, such orbits are atypical.

Fig. 14 shows snapshots of each OC at the end of the runs presented in Fig. 13. It should be understood that these results apply for an SFE of 25%. If this value is decreased to, say, 10%, the results may differ.

5.6. (90377) Sedna, 2000 CR₁₀₅ and 2003 UB₃₁₃

A fitting question is what fraction of objects are on orbits similar to those of (90377) Sedna, 2000 CR₁₀₅ and 2003 UB₃₁₃? First, a definition is needed of such orbits. The range in (a, e, i) space that was used to define objects on orbits similar to (90377) Sedna, 2000 CR₁₀₅ and 2003 UB₃₁₃ are given in Table 5. The runs were analyzed and the number of objects that fit the criteria were counted and stored separately. In order

Table 5

Region in (a, q, i) -space for objects to be classified as having orbits similar to those of 2003 UB₃₁₃, 2000 CR₁₀₅ and (90377) Sedna: this is used to create Fig. 15

Object	Range in a (AU)	Range in q (AU)	Range in i ($^{\circ}$)
2003 UB ₃₁₃	53–80	37–46	37–52
2000 CR ₁₀₅	200–300	40–50	15–30
Sedna	400–600	68–84	0–180

to improve statistics, the results were averaged over three time intervals, from 0.5 to 1.5 Myr, from 1.5 to 2.5 Myr and from 2 to 3 Myr. These final results are plotted in Fig. 15, which shows the percentage of objects on such orbits out of the total number of objects in the OC as a function of $\langle\rho\rangle$. Note the different scales on the vertical axis. This was done deliberately for clarity. The top panel is for objects on orbits similar to those of 2003 UB₃₁₃, the middle panel represents the fraction of objects similar to 2000 CR₁₀₅ and the bottom panel is for (90377) Sedna-like objects. The + symbols represent the first interval, the × symbols represent the second interval while the asterisks (*) are for the end of the runs.

From Fig. 15 one can directly determine what kind of average density one needs to produce objects like (90377) Sedna, 2000 CR₁₀₅ and 2003 UB₃₁₃ through this mechanism. It is clear that very few of these objects are produced

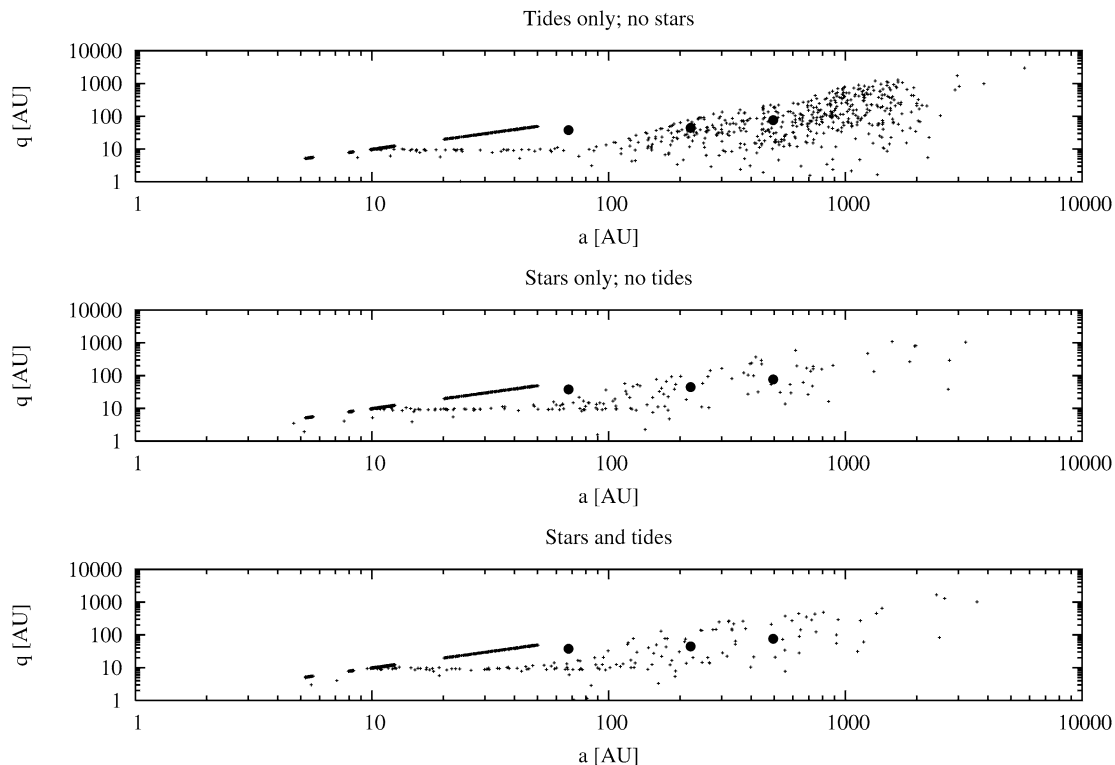


Fig. 14. Snapshots in a - q space at the end of the same runs used in Fig. 13. The top panel has tides only, the middle panel has stars only and the bottom panel has both stars and tides present. Note the large difference in efficiency between the cases.

when $\langle \rho \rangle \lesssim 10^3 M_{\odot} \text{pc}^{-3}$ and that the optimal density is $\langle \rho \rangle = 10^4$ – $10^5 M_{\odot} \text{pc}^{-3}$ for 2000 CR₁₀₅ and (90377) Sedna, though the latter is also present in runs with smaller density. 2003 UB₃₁₃, however, only seems to be produced in a few runs and only when the average density rivals the central value of the Trapezium cluster (see, e.g., Kroupa, 2000). 2000 CR₁₀₅ is a marginal case for $\langle \rho \rangle < 10^4$ while it is plausible that (90377) Sedna was created this way.

The remaining issue to be examined is the fate of the primordial Kuiper Belt.

5.7. Fate of the Kuiper Belt

Observations indicate that there is little material on low-eccentricity orbits beyond 50 AU in the Kuiper Belt. In addition, Gomes et al. (2004) suggested that the primordial Kuiper Belt must have been truncated at 30 AU to stop Neptune’s migration. Here we investigate the excitation of the primordial Kuiper Belt due to stellar encounters while the Sun was in an embedded cluster. In the simulations discussed above, two hundred test particles were placed on cold orbits from 20 to 50 AU to simulate this primordial Kuiper Belt.

The simulations contained a primordial Kuiper Belt, consisting of 200 comets spaced evenly between 20 and 50 AU. This Kuiper Belt was placed there to check whether or not it would get stirred up by passing stars during the runs. It is known (Kenyon and Bromley, 2002) that once the eccentricities of Kuiper Belt objects reach 0.05 or larger, the mutual collisions occur at velocities that shatter the objects rather than causing them to stick together. Therefore the Kuiper Belt was

examined at the end of the runs to check whether this condition occurred or not and if it did, at what value of semi-major axis. The analysis was performed as follows: at the end of the run, the comets in the Kuiper Belt were binned, with each bin containing ten comets. The mean eccentricity and standard deviation of the eccentricity were computed for each bin. The mean of the semi-major axis of comets in the bin was also computed. When the condition $\langle e \rangle > (0.05 - 1\sigma)$ was reached, the value of the semi-major axis was noted and taken as the cut-off value of the primordial Kuiper Belt.

This phenomenon of exciting the Kuiper Belt closer than 50 AU was observed in nine runs and are listed in Table 6. The columns are the run, and the two central densities for the clusters in which this phenomenon was observed. The first entry is the mean eccentricity at the cutoff point within 1σ of 0.05, the next value is the standard deviation, σ , and the third entry is the value of the semi-major axis at which this cutoff occurred. The entries < 20 mean that the stirring occurred to within 20 AU. When the letters ‘UB’ are written after the semi-major axis value, it indicates that the run produced a 2003 UB₃₁₃-like object. In all cases the eccentricities of Jupiter and Saturn were checked at the end of the simulations as well and it turned out that Saturn’s eccentricity is the range from 0.01–0.05.

In many cases no excitation was discovered within 50 AU. In order to determine what sort of mean density is needed to excite the Kuiper Belt down to about 50 AU, some runs were repeated with a Kuiper Belt ranging from 20 to 100 AU. The entries for these additional runs are given in parenthesis.

As can be seen from Table 6, the cutoff point varies from < 20 AU to about 40 AU. In each of the runs where the

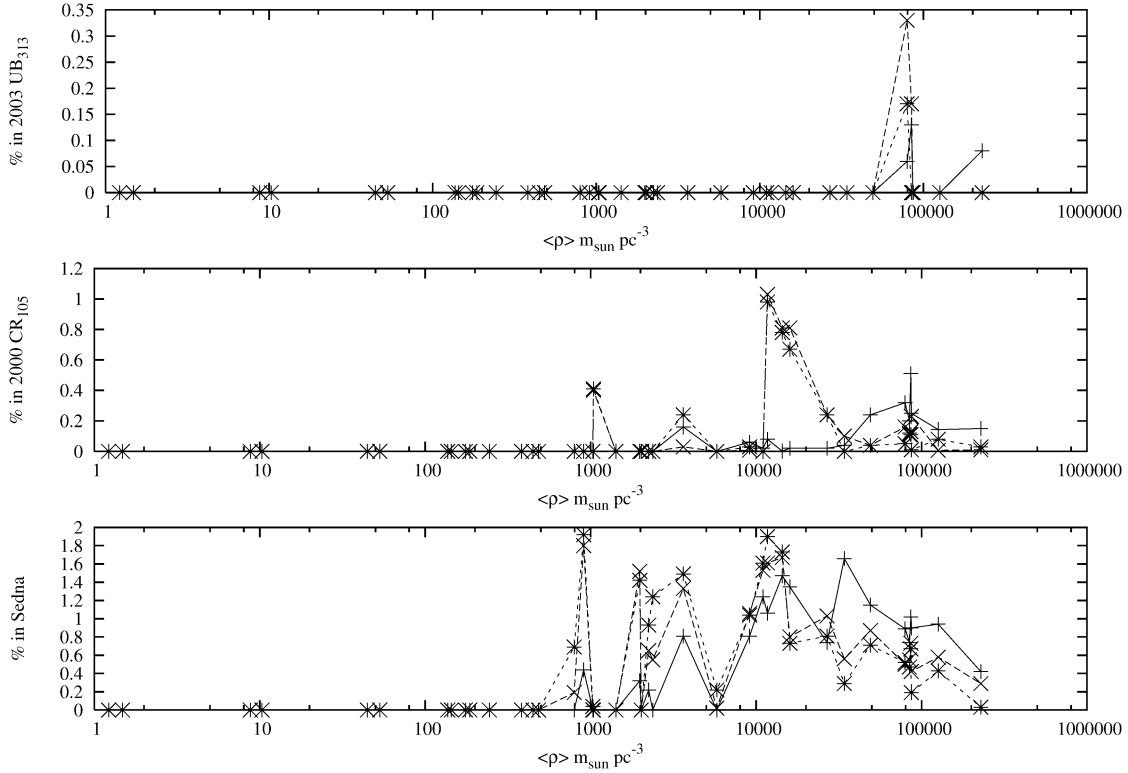


Fig. 15. A plot of the fraction of objects in the OC on orbits similar to those of 2003 UB₃₁₃ (top panel), 2000 CR₁₀₅ (middle panel) and (90377) Sedna (bottom panel) as a function of mean density $\langle \rho \rangle$. The + symbols are taken from $t = 0.5\text{--}1.5$ Myr, the \times symbols are from $t = 1.5\text{--}2.5$ Myr and the asterisks * are sampled from $t = 2.0\text{--}3.0$ Myr. It is obvious that 2000 CR₁₀₅ and 2003 UB₃₁₃ are only created when the mean density is $\gtrsim 10^4$ (see text for a further discussion).

Table 6

The eccentricity, standard deviation in eccentricity and semi-major axis at which the primordial Kuiper Belt got dynamically excited

Run	10^5	10^6
1	(> 100)	–
2	0.0480, 0.020, 35.8	–
3	0.0485, 0.0138, 29.1	0.0416, 0.0215, 40.6
4	(0.0441, 0.0248, 93.1)	0.0525, 0.0156, 28.5
5	(> 100)	(0.0534, 0.0311, 69.9)
6	(0.0491, 0.0182, 82.6)	<20
7	(> 100)	<20 UB
8	(> 100)	<20 UB
9	(> 100)	0.0484, 0.0204, 21.0 UB
0	(> 100)	0.0473, 0.0130, 20.8

On top are the two central densities of the clusters for which this occurred and on the left are the run number. The first entry is the mean eccentricity within a 1σ value of 0.05, the second entry is the standard deviation of the eccentricity in that bin and the third is the semi-major axis at which this occurred. An entry <20 means that even at 20 AU the Kuiper Belt was stirred to eccentricities >0.05 . An entry ‘UB’ means a 2003 UB₃₁₃-like object was created during that run.

Kuiper Belt was stirred up, there were (90377) Sedna-like and 2000 CR₁₀₅-like objects. However, in most of the runs for clusters with $\rho_0 = 10^5 M_{\odot} \text{pc}^{-3}$, objects similar to these two were reproduced, so that it is possible to form both (90377) Sedna and 2000 CR₁₀₅ without stirring the Kuiper Belt interior to 50 AU. In addition, [Morbidelli and Levison \(2004\)](#) find that if the cluster was very dense, it would create an inner edge of the OC close to the Sun. Since objects with q in the range 40–80 are rare with $a < 200$ AU, this favors a less dense star cluster. Last,

in all the runs whenever a 2003 UB₃₁₃-like object is produced, the Kuiper Belt is excited at 20 AU or less. In other words it appears unlikely that one can produce an object like 2003 UB₃₁₃ and leave the Kuiper Belt intact and the observations seem to favor a looser cluster ([Morbidelli and Levison, 2004](#)).

The question of what mean density is needed to instigate collisional grinding of the Kuiper Belt at 50 AU is difficult to determine from our simulations. The excitation occurs because of a close stellar passage and is therefore not only dependent on the mean density but also on time. For each run the Kuiper Belt’s was tabulated as a function of the mean density. It was found that there was $\gtrsim 50\%$ chance that the eccentricities at 50 AU exceeded 0.05 when $\langle \rho \rangle \gtrsim 10^5 M_{\odot} \text{pc}^{-3}$. To excite it to the same levels at 30 AU required mean densities of a factor of a few larger.

6. Conclusions

Computer simulations have been performed of the formation of the OC from comets starting in the pre-LHB Jupiter–Saturn region while the Sun was in an embedded star cluster. The tidal field caused by the cluster gas and stellar passages are taken into account, as is the orbit of the Sun itself in the Plummer potential of the cluster. The simulations showed that:

1. About 2–18% of the initial sample of comets from 4 to 12 AU ended up in the OC after 3 Myr.
2. The solar eccentricity and mean distance play a role in the overall efficiency of creating the OC since it deter-

mines $\langle \rho \rangle$, which is the leading parameter. Since stellar perturbations dominate for larger densities, the solar inclination is of lesser importance.

3. (90377) Sedna can be reproduced within a few Myr for $\langle \rho \rangle \gtrsim 10^3 M_\odot \text{pc}^{-3}$. In order to reproduce 2000 CR₁₀₅, mean densities of $10^4 M_\odot \text{pc}^{-3}$ or higher are needed.
4. Based on the simulations performed, 2003 UB₃₁₃ cannot have formed by this mechanism without exciting and subsequently destroying the Kuiper Belt to 20 AU or less.
5. The computations produce many OC objects on retrograde orbits; in fact, the OC is fairly isotropic for $\langle r \rangle \gtrsim r_{50}$.
6. When $\langle \rho \rangle \gtrsim 10 M_\odot \text{pc}^{-3}$, the median distance of the comet from the Sun scales approximately as $r_{50} \propto \langle \rho \rangle^{-1/2}$.
7. The stars play a more prominent role for large densities, where they are more destructive to the OC, too. For small densities the tides are more important in shaping the OC.

Acknowledgments

The authors wish to thank Luke Dones and Alessandro Morbidelli as well as the reviewers Julio A. Fernández and Fred Adams for constructive criticism in improving this manuscript. R.B. and M.J.D. thank the Natural Sciences and Engineering Research Council (NSERC) of Canada for its partial support in funding this research. R.B. also acknowledges funding from the Canadian Institute for Theoretical Astrophysics (CITA) through their National Fellows programme. H.F.L. is supported by NASA's PGG and Origins programmes.

Appendix A. Derivation of tidal influence on comets

Define the position vector of the Sun relative to the cluster centre to be \vec{r}_\odot , the position vector of the comet to be \vec{r}_c and the heliocentric position of the comet is $\vec{d} = \vec{r}_c - \vec{r}_\odot$. Taking the cluster centre to be fixed, for a comet with mass m_c at position \vec{r}_c and the Sun of mass m_\odot at position \vec{r}_\odot , one has the equations of motion

$$\begin{aligned} m_\odot \ddot{\vec{r}}_\odot &= -\frac{GM_\odot M \vec{r}_\odot}{(r_\odot^2 + c^2)^{3/2}} - \frac{Gm_\odot m_c (\vec{r}_\odot - \vec{r}_c)}{|\vec{r}_\odot - \vec{r}_c|^3}, \\ m_c \ddot{\vec{r}}_c &= -\frac{Gm_c M \vec{r}_c}{(r_c^2 + c^2)^{3/2}} - \frac{Gm_\odot m_c (\vec{r}_c - \vec{r}_\odot)}{|\vec{r}_c - \vec{r}_\odot|^3}. \end{aligned} \quad (\text{A.1})$$

This can be reduced to

$$\begin{aligned} \ddot{\vec{d}} + \frac{G(m_\odot + m_c) \vec{d}}{d^3} &= \frac{GM \vec{r}_\odot}{(r_\odot^2 + c^2)^{3/2}} \\ &\quad - \frac{GM(\vec{r}_\odot + \vec{d})}{(|\vec{r}_\odot + \vec{d}|^2 + c^2)^{3/2}}. \end{aligned} \quad (\text{A.2})$$

One can write the right-hand side as ∇R , where R is the disturbing function, given by

$$R = \frac{GM}{\sqrt{|\vec{r}_\odot + \vec{d}|^2 + c^2}} + \frac{GM(\vec{r}_\odot \cdot \vec{d})}{(r_\odot^2 + c^2)^{3/2}}. \quad (\text{A.3})$$

In general $|\vec{d}| \ll |\vec{r}_\odot|$ so that one can expand R in terms of \vec{d} to give

$$\begin{aligned} R &\approx \frac{GM}{\sqrt{r_\odot^2 + c^2}} \left[1 - \frac{d^2}{2(r_\odot^2 + c^2)} \right. \\ &\quad \left. + \frac{3(\vec{r}_\odot \cdot \vec{d})^2}{2(r_\odot^2 + c^2)^2} \right] + O(d^3). \end{aligned} \quad (\text{A.4})$$

It can be proven that in the limit $c \rightarrow 0$ and $M_\odot \ll M$ Eq. (A.4) reduces to the disturbing function for two interacting point masses (see, e.g., Kinoshita and Nakai, 1999). If the Sun is on a circular orbit, the disturbing function can be averaged over both the motion of the comet and the Sun. Assuming the Sun's orbital plane about the cluster centre defines the reference plane for the comet's orbit, one has

$$\begin{aligned} \mathcal{R} &= \gamma \left[15e^2 \sin^2 \eta \cos 2\omega \right. \\ &\quad \left. + (2 + 3e^2)(3 \cos^2 \eta - 1 - 4\zeta^2) \right], \end{aligned} \quad (\text{A.5})$$

where η is the comet's inclination, and the comet's other elements are heliocentric and have their usual notation. In Eq. (A.5) the parameter ζ is defined as $\zeta = c/r_\odot$ and, following Kinoshita and Nakai (1999),

$$\gamma = \frac{n_\odot^2 a^2}{16(1 + \zeta^2)}, \quad (\text{A.6})$$

where the mean angular motion of the Sun's orbit, n_\odot , satisfies

$$n_\odot^2 = \frac{GM}{r_\odot^3 (1 + \zeta^2)^{3/2}}. \quad (\text{A.7})$$

The equations of motion derived from Eq. (A.5), with the use of Lagrange's planetary equations (Murray and Dermott, 1999), of the variables e , ω and η become

$$\frac{de}{d\tau} = -30e\sqrt{1 - e^2} \sin^2 \eta \sin 2\omega, \quad (\text{A.8})$$

$$\frac{d\eta}{d\tau} = -\frac{15e^2 \sin 2\eta \sin 2\omega}{\sqrt{1 - e^2}}, \quad (\text{A.9})$$

$$\frac{d\omega}{d\tau} = \frac{6[5 \cos 2\omega (\sin^2 \eta - e^2) + 5 \cos^2 \eta - (1 - e^2)(1 + 4\zeta^2)]}{\sqrt{1 - e^2}}, \quad (\text{A.10})$$

where we implicitly introduced a characteristic frequency, Γ , given by

$$\Gamma = \frac{\gamma}{na^2} = \frac{n_\odot^2}{16n(1 + \zeta^2)}, \quad (\text{A.11})$$

where n is the mean angular motion of the comet around the Sun,

$$n^2 = \frac{GM_\odot}{a^3} \quad (\text{A.12})$$

and where we used $\tau = \Gamma t$. From Eq. (A.10) one can derive that $h = (1 - e^2) \cos^2 \eta$, the z -component of the angular momentum, is a constant by solving

$$\frac{de}{d\eta} = \frac{1 - e^2}{e} \tan \eta. \quad (\text{A.13})$$

To transform to a Solar System inclination, i , one uses $\cos \eta = \cos i \cos i_{\odot} + \sin i \sin i_{\odot} \cos(\Omega - \Omega_{\odot})$ where the reference plane is the invariable plane of the Solar System, and i_{\odot} is the inclination of the Sun's orbit with respect to its orbital plane.

There are two limiting cases: $r_{\odot} \gg c$ ($\zeta \rightarrow 0$) and $r_{\odot} \ll c$ ($\zeta \rightarrow \infty$). In the former case, it can easily be shown that the averaged disturbing function reduces to that of the Kozai mechanism (Kozai, 1962) while in the latter case the disturbing function reduces to that of a homogeneous sphere. The analytical solution of e , η and ω shall be explored in more detail.

A.1. Case where $\zeta < 1$

Following Kinoshita and Nakai (1999) introduce the variable $x = 1 - e^2$ so that $h = x \cos^2 \eta$. The constant of motion can be written as

$$C = 15(1-x)(1-h/x) \cos 2\omega + (5-3x)(3h/x - 1 - 4\zeta^2). \quad (\text{A.14})$$

A.1.1. Circulation of ω

At the time $\omega = 0$ define $x = x_0$ and $\eta = \eta_0$, and thus x_0 is the maximum value of x and thus a minimum in e . Substituting into Eq. (A.14) one has

$$\cos 2\omega = \frac{-(1+4\zeta^2)x^2 + [5(1+h) - 4x_0(1-\zeta^2)]x - 5h}{5(1-x)(x-h)}, \quad (\text{A.15})$$

so that

$$\sin^2 \omega = \frac{2x(1-\zeta^2)(x_0-x)}{5(1-x)(x-h)}, \quad (\text{A.16})$$

$$\cos^2 \omega = \frac{(3+2\zeta^2)(x_2-x)(x-x_1)}{5(1-x)(x-h)}, \quad (\text{A.17})$$

where

$$x_1 + x_2 = \frac{5(1+h) - 2x_0(1-\zeta^2)}{3+2\zeta^2}, \quad (\text{A.18})$$

$$x_1 x_2 = \frac{5h}{3+2\zeta^2}, \quad (\text{A.19})$$

and $x_1 < x_2$. Physically x_1 is the minimum value of x during one revolution of ω and thus corresponds to the maximum eccentricity e_1 . The other root is physically meaningless. From Lagrange's planetary equations

$$\frac{dx}{d\tau} = -\frac{15}{2(1+\zeta^2)} \frac{(1-x)(x-h)}{\sqrt{x}} \cos \omega \sin \omega, \quad (\text{A.20})$$

which reduces to

$$\frac{dx}{d\tau} = -\frac{3\sqrt{2}}{2(1+\zeta^2)} \sqrt{(3+2\zeta^2)(1-\zeta^2)} \times \sqrt{(x_2-x)(x_0-x)(x-x_1)}, \quad (\text{A.21})$$

which is the same form as that of Kinoshita and Nakai (1999) and reduces to their Eq. (20) when $\zeta = 0$. The solution to

Eq. (A.21) can be written as

$$x = x_0 + (x_1 - x_0) \operatorname{cn}^2(\theta, k), \quad (\text{A.22})$$

or, in terms of eccentricities

$$e^2 = e_0^2 + (e_1^2 - e_0^2) \operatorname{cn}^2(\theta, k), \quad (\text{A.23})$$

where

$$\theta = \frac{2\mathcal{K}(k)}{\pi} \left(vt + \frac{\pi}{2} \right), \quad (\text{A.24})$$

$$v = \frac{3\sqrt{2}\pi\Gamma}{8\mathcal{K}(k)(1+\zeta^2)} \sqrt{e_1^2 - e_2^2} \sqrt{(3+2\zeta^2)(1-\zeta^2)}, \quad (\text{A.25})$$

$$k = \sqrt{\frac{e_1^2 - e_0^2}{e_1^2 - e_2^2}}, \quad (\text{A.26})$$

where $\mathcal{K}(k)$ is the complete elliptic integral of the first kind. It should be noted that when one plots the solutions for x and e they are out of phase by π . Following Kinoshita and Nakai (1999), the normalized period of the argument of pericentre becomes

$$\bar{P}_{\omega} = \frac{8\sqrt{2}(1+\zeta^2)\mathcal{K}(k)}{3\sqrt{e_1^2 - e_2^2} \sqrt{(3+2\zeta^2)(1-\zeta^2)}}. \quad (\text{A.27})$$

A.1.2. Libration of ω

In the case ω librates, there are two values of the eccentricity for each value of ω . As such, e_0 is the smaller eccentricity at $\omega = 90^\circ$ and at $t = 0$. From Eq. (A.14) one has

$$\cos 2\omega = \frac{-(1+4\zeta^2)x^2 + [5(1+h) + \frac{10h}{x_0} - 4x_0\zeta^2 + 6x_0]x - 5h}{5(1-x)(x-h)}, \quad (\text{A.28})$$

so that

$$\sin^2 \omega = \frac{2x(1-\zeta^2)(x_2-x)}{5(1-x)(x-h)}, \quad (\text{A.29})$$

$$\cos^2 \omega = \frac{(3+2\zeta^2)(x_0-x)(x-x_1)}{5(1-x)(x-h)}, \quad (\text{A.30})$$

where

$$x_1 = \frac{5h}{x_0(3+2\zeta^2)}, \quad (\text{A.31})$$

$$x_2 = \frac{1}{2(1+\zeta^2)} \left[5 \left(1 + h - \frac{h}{x_0} \right) - x_0(3+2\zeta^2) \right].$$

Now

$$x_2 - x_0 = \frac{5(1-x_0)(x_0-h)}{2x_0(1-\zeta^2)} > 0, \quad (\text{A.32})$$

so that $x_2 > x_0$. Therefore, the differential equation for x is the same as Eq. (A.21). However, the solution is slightly different, since

$$e^2 = e_0^2 + (e_1^2 - e_0^2) \operatorname{cn}^2(\theta, k), \quad (\text{A.33})$$

with

$$\theta = \frac{2\mathcal{K}(k)}{\pi}(vt + \pi), \quad (\text{A.34})$$

$$v = \frac{3\sqrt{2}\pi\Gamma}{8\mathcal{K}(k)(1+\zeta^2)}\sqrt{e_1^2 - e_2^2}\sqrt{(3+2\zeta^2)(1-\zeta^2)}, \quad (\text{A.35})$$

$$k = \sqrt{\frac{e_1^2 - e_0^2}{e_1^2 - e_2^2}}. \quad (\text{A.36})$$

The period of ω is computed in the same way for the case of circulation.

For the librating case, the maximum eccentricity is

$$e_1 = \sqrt{1-x_1} = \sqrt{1 - \frac{5\cos\eta_1}{3+2\zeta^2}}, \quad (\text{A.37})$$

so that the critical inclination becomes

$$\eta_c = \arccos\left(\sqrt{\frac{3+2\zeta^2}{5}}\right).$$

As $\zeta \rightarrow 0$ one is back to the classical Kozai mechanism and $\eta_c = 39.23^\circ$. But as $\zeta \rightarrow 1$, $\eta_c \rightarrow 0$, so that when the Sun is close to the Plummer radius, the mutual inclination between the comet and the Sun's orbit needs to be very small for the comets to librate in ω . The turning points of ω occur when $\dot{\omega} = 0$, which can be solved to give

$$\cos 2\omega_c = \frac{5h - x^2(1+4\zeta^2)}{5(h-x^2)}. \quad (\text{A.38})$$

When $\zeta \rightarrow 0$ one is back to the classical Kozai regime. However, as $\zeta \rightarrow 1$ then the libration width increases to 90° .

The above analysis was done where the Sun's orbit is circular and ζ is a constant. It is shown that most torquing happens when $\zeta \sim 1$. To solve for the case when $\zeta > 1$, the roots x_1 and x_2 need to be switched and the libration of ω revolves in the opposite direction. Apart from that, the behavior is the same.

If we allow ζ to vary, the above analysis is no longer correct, but does give insight into possible features of the motion. Variations in ζ will cause the values of e_1 and e_2 to change, both in the case where ω librates or circulates, so that switching between these two regimes is possible. The variations in e , modeled by Eq. (A.23), will now be a function of the Sun's orbit. Hence the contours in the e - ω portraits pulse themselves with time and the libration islands widen and narrow in a quasi-periodic manner.

A.2. Case where $\zeta = 1$

The case where $\zeta = 1$ is special and even though its solution contains singularities, it will be listed here for purpose of completeness. Substituting $\zeta = 1$ in the case where ω circulates yields no solution, so that circulation is not possible in this case. As such, one proceeds from the librating case. Then

$$\cos 2\omega = \frac{-x^2 + [\frac{2h}{x_0} + 2x_0 - (1+h)]x - h}{(1-x)(x-h)}, \quad (\text{A.39})$$

so that

$$\sin^2 \omega = \frac{xx_2}{(1-x)(x-h)}, \quad (\text{A.40})$$

$$\cos^2 \omega = \frac{(x_0-x)(x-x_1)}{(1-x)(x-h)}, \quad (\text{A.41})$$

where

$$x_1 = \frac{h}{x_0}, \quad (\text{A.42})$$

$$x_2 = 1 + h - x_0 - \frac{h}{x_0}. \quad (\text{A.43})$$

Thus

$$\frac{dx}{d\tau} = -\frac{15}{4}\sqrt{x_2(x_0-x)(x-x_1)}, \quad (\text{A.44})$$

which can be solved to give

$$x = \frac{1}{2} \cot \theta \left[1 + (x_0 + x_1) \tan \theta - \sqrt{1 + (x_0 - x_1)^2 \tan^2 \theta} \right], \quad (\text{A.45})$$

where

$$\theta = \frac{15\sqrt{x_2}\Gamma}{4}t.$$

It should be noted that the above solution in Eq. (A.45) has never been witnessed in the numerical simulations. The reason is that this solution is attitude unstable so that one will always witness a librating or circulating solution that contains no singularities like the one above.

A.3. Case where $\zeta > 1$

To solve the case where $\zeta > 1$, one needs to avoid running into quantities becoming imaginary when the term $1 - \zeta^2$ becomes negative. Fortunately, there is a way out. Differentiating Eq. (A.28) with respect to x and solving for ζ one finds

$$\left\{ \frac{d \cos 2\omega}{dx} \right\}_{\omega=0} = 0, \quad (\text{A.46})$$

when $\zeta = \pm 1$. Additionally,

$$\left\{ \frac{d^2 \cos 2\omega}{dx^2} \right\}_{\omega=0} = 0 \quad (\text{A.47})$$

also yields $\zeta = \pm 1$. Hence, contrary to the classical Kozai mechanism, where e is a minimum when $\omega = 0$, it is now a maximum, since there is a point of inflexion when $\zeta = 1$. Originally x_0 was defined to be a maximum and $x_1 < x_2$. Since the former statement is no longer true but the latter is, one needs to exchange the roots x_1 and x_2 in Eqs. (A.21) and (A.23). Therefore, in principle the solution to the problem is the same, with libration and circulation still occurring, but now the libration regions appear below the circulation ones in the e - ω portraits.

This is demonstrated in Figs. 16–18, where the contours in the q - ω plane have been plotted for different values of $\zeta = 0.5$ (Fig. 16), $\zeta = 1$ (Fig. 17) and $\zeta = 2$ (Fig. 18). Note that in the case where $\zeta = 1$ there is no circulation. Additionally, note that the circulation regions for $\zeta = 0.5$ and $\zeta = 2$ are on opposite sides of the libration regions, confirming our theory.

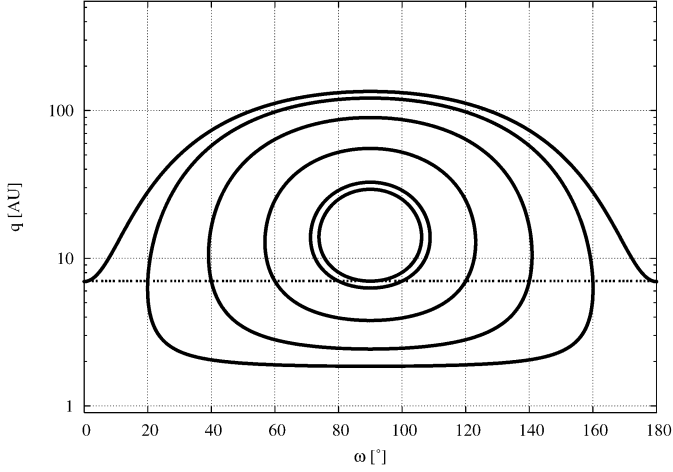


Fig. 16. Contour levels of the disturbing function in q - ω space for $\zeta = 0.5$ ($r_\odot > c$).

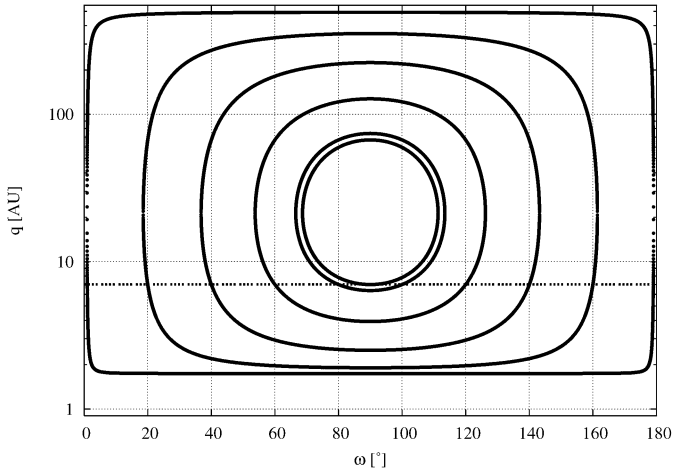


Fig. 17. Contour levels of the disturbing function in q - ω space for $\zeta = 1$ ($r_\odot = c$).

Appendix B. Derivation of tidal torquing time, t_q

Here the formula for t_q is derived for the adapted tidal model from Eq. (A.10). One has

$$\dot{e} = -30\Gamma e \sqrt{1-e^2} \sin^2 \eta \sin 2\omega. \quad (\text{B.1})$$

Now $\dot{q} = \dot{a}(1-e) - a\dot{e}$ and, for the secular evolution, $\dot{a} = 0$. Additionally $e \sim 1$, so that $\sqrt{1-e^2} \approx \sqrt{2q/a}$. Then

$$\dot{q} = 30\Gamma \sqrt{2qa} \sin^2 \eta \sin 2\omega. \quad (\text{B.2})$$

DQT87 use $\langle \sin 2\omega \rangle = \sqrt{2}/2$, which is adopted here as well. Hence

$$\dot{q} = 30\Gamma \sin^2 \eta \sqrt{qa}. \quad (\text{B.3})$$

Substituting Eqs. (A.11) and (A.7) into Eq. (B.3) and using Eq. (2), one has, after some simplification

$$\dot{q} = \frac{5\pi\sqrt{q}}{2} \sin^2 \eta G\rho_0 \frac{a^2}{\sqrt{GM_\odot}} \frac{\zeta^3}{(1+\zeta^2)^{5/2}}. \quad (\text{B.4})$$

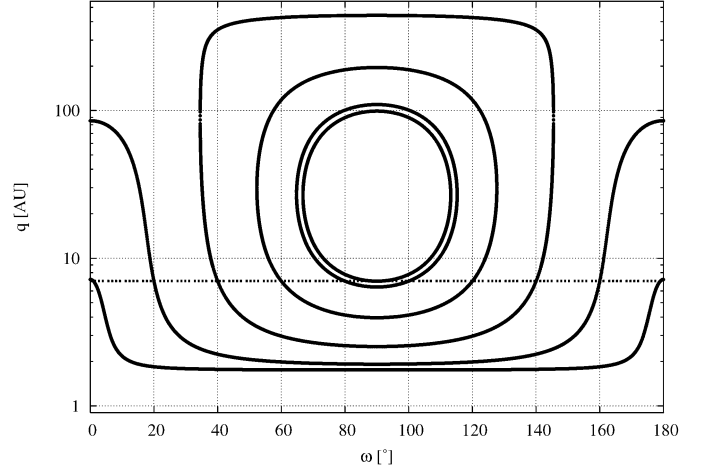


Fig. 18. Contour levels of the disturbing function in q - ω space for $\zeta = 2$ ($r_\odot < c$).

Now $t_q = \Delta q / \dot{q}$. When changing units so that $G = 1$, and a is measured in AU, then $M_\odot = 4\pi^2$ and one eventually obtains

$$t_q = 1.78 \times 10^{-2} \frac{\Delta q}{\sqrt{q}} \times \csc^2 \eta \left(\frac{10^3}{a} \right)^2 \left(\frac{10^4}{\rho_0} \right) \frac{(1+\zeta^2)^{5/2}}{\zeta^3},$$

which is the same as Eq. (6) and the unit of time is Myr.

Appendix C. Precession of (90377) Sedna

The precession frequency of (90377) Sedna and Sedna-like objects can be roughly computed by treating the perturbations of the jovian planets as an artificial J_2 coefficient of the Sun. This coefficient is computed as (see, e.g., Murray and Dermott, 1999)

$$J_2 = \frac{1}{2} \sum_{i=1}^4 \frac{m_i}{M_\odot} \left(\frac{a_i}{R_\odot} \right)^2, \quad (\text{C.1})$$

which, for the current configuration of the jovians, gives approximately $J_2 = 2.054 \times 10^3$. The induced precession frequency of the argument of pericentre and node, averaged over the mean anomaly, are given by

$$\dot{\omega} = \frac{3n}{4} \left(\frac{R_\odot}{a} \right)^2 J_2 \frac{5 \cos^2 i - 1}{(1-e^2)^2}, \quad (\text{C.2})$$

$$\dot{\Omega} = -\frac{3n}{2} \left(\frac{R_\odot}{a} \right)^2 J_2 \frac{\cos i}{(1-e^2)^2}, \quad (\text{C.3})$$

where n is the mean motion. Substituting the obtained value of J_2 and using $a = 500$ AU and (90377) Sedna's inclination and eccentricity, the precession period for ω computes to be about 1.87 Gyr, which is in reasonable agreement with numerical simulations. The period of regression for Ω is 3.67 Gyr, again in good agreement with numerical simulations. From DQT87 the precession period induced by the Galactic Tide is computed to be of order 100 Gyr. Therefore, the planetary effects dominate today.

Appendix D. Distribution of changes in orbital energy

From DQT87 one knows that the scattering process by Jupiter and Saturn becomes a simple one once $a \gg q$, since the perturbations in energy are much more significant than those in q and i and the encounters are uncorrelated. The energy kicks occur at pericentre and since q remains approximately fixed if no close approach occurs, the energy perturbations are a random walk process.

From the works of Fernández (1981) as well as DQT87, one knows what the root-mean-square kick in energy is as a function of q for the current planetary configuration, given a value of i . However, since one deals with the pre-LHB system, one cannot guarantee that the energy kicks are the same as in the current configuration for a given q and i . Also, in principle the rms value is undefined, but can be defined if the number of scattering experiments is finite.

Therefore a simple experiment was set up to determine the root-mean-square kicks for the pre-LHB configuration, including Uranus and Neptune, and these were compared to the current configuration and the values obtained by DQT87: a system was set up consisting of the giant planets and 10^4 test particles with $a = 10^3$ AU and $q \in [4, 38]$ AU and i was sinusoidally chosen in the interval $i \in [0^\circ, 30^\circ]$, to be consistent with DQT87. There were 270 particles per value of q and these were started randomly on their orbits at a distance $r \in [40, 100]$ AU to account for randomness in the planets' positions. The change in energy after their pericentre passage was computed as $x = |1/a - 1/a_0|$. The root-mean-square value over all 270 particles per value of q was used as the typical energy kick, u .

The results are shown in Fig. 2. Due to the more compact configuration of the pre-LHB system, the value of the root-mean-square kick falls off much more rapidly than in the current configuration, as is expected. However, up to $q \sim 15$ AU, the typical value of u for both systems is rather similar. It is only beyond this distance that the two systems differ significantly.

The reader should be made aware that the distribution of kicks from a planet as a function of u is highly non-Gaussian (Everhart, 1968). For a Gaussian distribution the rms value is ~ 1.5 the median value. For the observed distribution of kicks, this factor is close to 6 (Everhart, 1968) and is caused by the long tail of the distribution, which goes as $|u|^{-3}$. Everhart's (1968) distribution is

$$h(u) = Ae^{-(B|u|-1)^2} + \frac{C}{(D^2 + u^2)^{3/2}}, \quad (\text{D.1})$$

where the parameters A , B , C and D are determined from experiment. The parameter A is chosen so that the distribution is properly normalized. The normalized cumulative distribution is therefore

$$H(u) = \frac{A\sqrt{\pi}}{2B} \left(\text{erf}(B|u| - 1) + \text{erf}(1) \right) + \frac{Cu}{D^2\sqrt{D^2 + u^2}}, \quad (\text{D.2})$$

while one can compute a mean kick for positive values of u only, the rms value is undefined since the integral $\int u^2 h(u) du$ diverges logarithmically (see Eq. (D.4) below).

The mean value of $|u|$ is computed as

$$\langle |u| \rangle = \int_0^\infty u h(u) du = \frac{A}{2B^2} \left(\sqrt{\pi} (1 + \text{erf}(1)) + e^{-1} \right) + \frac{C}{D}. \quad (\text{D.3})$$

However, the value of $\langle u^2 \rangle$ needs to be computed from

$$\int_0^\infty u^2 h(u) du = \frac{3A\sqrt{\pi} \text{erf}(Bu - 1)}{4B^3} - \frac{A}{2B^2} e^{-(Bu-1)^2} \left(u + \frac{1}{B} \right) - \frac{Cu}{\sqrt{D^2 + u^2}} + C \ln \left(u + \sqrt{D^2 + u^2} \right) \Big|_0^\infty, \quad (\text{D.4})$$

which diverges logarithmically. In principle the upper limit of integration is not infinity since one is limited to the physical radius of the planet, but because of the logarithmic term, the rms value increases as $\sqrt{\ln(N)}$, where N is the number of scattering experiments. DQT87 was aware of both these issues and took the observed rms value as a function of q computed after a fixed number of experiments, and obtained results similar to Fig. 2.

However, since the rms value poorly defined, it shall not be used here but a substitute value is found: by using parameters from Everhart (1968) that are typical to the problem, it is determined that the distribution becomes highly non-Gaussian when $u \sim 4GM_p/a_p$ and define $u_0 = GM_p/a_p$. Here the tail of the distribution begins to dominate and for this value of u the normalized cumulative function $H(u) \sim 0.74$, so that there is approximately a 25% chance a comet gets a kick $u \geq 4u_0$. Even though the most frequent kicks are of order u_0 , it is the infrequent, large kicks that dominate the motion: under the diffusion approximation it would take 16 passages with kicks of u_0 to where one kick of $4u_0$ takes the comet directly and this happens after about four passages. Therefore a new value for the typical kick other than the poorly-defined rms value is needed.

For the current distribution the average value, $\langle |u| \rangle \sim 8u_0$, so that the typical kick is $|u| \in (4u_0, 8u_0)$. As it turns out, the mean value, $\langle |u| \rangle$, corresponds well with the rms value of DQT87 and those found in the present work. It is this mean value that has been used to compute the value of t_d in Fig. 3.

References

- Adams, F.C., Bloch, A.M., 2005. Orbits in extended mass distributions: General results and the spirographic approximation. *Astrophys. J.* 629, 204–218.
- Adams, F.C., Laughlin, G., 2001. Constraints on the birth aggregate of the Solar System. *Icarus* 150, 151–162.
- Adams, F.C., Proszkow, E.M., Fatuzzo, M., Myers, P.C., 2006. Early evolution of stellar groups and clusters: Environmental effects on forming planetary systems. *Astrophys. J.* 641, 504–525.
- André, P., 2002. Nearby protoclusters as laboratories for understanding star formation on galactic scales. *Astron. Astrophys.* 281, 51–66.
- Bally, J., Yu, K.C., Rayner, J., Zinnecker, H., 1998. Hubble space telescope wide field planetary camera 2 observations of the young bipolar H II region S106. *Astron. J.* 116, 1868–1881.
- Binney, J., Tremaine, S., 1987. *Galactic Dynamics*. Princeton Univ. Press, Princeton, NJ.

- Brown, M.E., Trujillo, C., Rabinowitz, D., 2004. Discovery of a candidate inner Oort Cloud planetoid. *Astrophys. J.* 617, 645–649.
- Brown, M.E., Trujillo, C.A., Rabinowitz, D.L., 2005. Discovery of a planet-sized object in the scattered Kuiper Belt. *Astrophys. J.* 635, L97–L100.
- Dones, L., Weissman, P.R., Levison, H.F., Duncan, M.J., 2004. Oort Cloud formation and dynamics. In: Johnstone, D., Adams, F.C., Lin, D.N.C., Neufeld, D.A., Ostriker, E.C. (Eds.), *ASPC*, vol. 324. ASP, San Francisco.
- Duncan, M.J., Levison, H.F., 1997. A scattered comet disk and the origin of the Jupiter family comets. *Science* 276, 1670–1672.
- Duncan, M., Quinn, T., Tremaine, S., 1987. The formation and extent of the Solar System comet cloud. *Astron. J.* 94, 1330–1338.
- Eggers, S., 1999. *Cometary Dynamics During the Formation of the Solar System*, Ph.D. thesis, Mathematisch-Naturwissenschaftlichen Fakultäten der Georg-August-Universität, Göttingen.
- Everhart, E., 1968. Change in total energy of comets passing through the Solar System. *Astron. J.* 73, 1039–1052.
- Fernández, J.A., 1981. New and evolved comets in the Solar System. *Astron. Astrophys.* 96, 26–35.
- Fernández, J.A., 1997. Formation of the Oort Cloud and the primitive galactic environment. *Icarus* 129, 106–119.
- Fernández, J.A., Brunini, A., 2000. The buildup of a tightly bound comet cloud around an early Sun immersed in a dense galactic environment: Numerical experiments. *Icarus* 145, 580–590.
- Fernández, J.A., Gallardo, T., Brunini, A., 2004. The scattered disk population as a source of Oort Cloud comets: Evaluation of its current and past role in populating the Oort Cloud. *Icarus* 172, 372–381.
- Gaidos, E.J., 1995. *Paleodynamics: Solar System formation and the early environment of the Sun*. *Icarus* 114, 258–268.
- Gladman, B., Holman, M., Grav, T., Kavelaars, J., Nicholson, P., Aksnes, K., Petit, J.-M., 2002. Evidence of an extended scattered disk. *Icarus* 157, 269–279.
- Gomes, R.S., Morbidelli, A., Levison, H.F., 2004. Planetary migration in a planetesimal disk: Why did Neptune stop at 30 AU? *Icarus* 170, 492–507.
- Gomes, R.S., Gallardo, T., Fernández, J.A., Brunini, A., 2005. On the origin of the high-perihelion scattered disk: The role of the Kozai mechanism and mean-motion resonances. *Celest. Mech. Dynam. Astron.* 91, 109–129.
- Guthermuth, R.A., Megeath, S.T., Pipher, J.L., Williams, J.P., Allen, L.E., Myers, P.C., Raines, S.N., 2005. The initial configuration of young stellar clusters: A *K*-band number counts analysis of the surface density of stars. *Astrophys. J.* 632, 397–420.
- Heisler, J., Tremaine, S., 1986. The influence of the galactic tidal field on the Oort comet cloud. *Icarus* 65, 13–26.
- Heggie, D.C., Hut, P., 1993. Binary–single-star scattering. IV. Analytic approximations and fitting formulae for cross sections and reaction rates. *Astrophys. J. Suppl. Ser.* 85, 347–409.
- Henriksen, R.N., 1986. Star formation in giant molecular clouds. *Astrophys. J.* 310, 189–206.
- Hills, J.G., 1981. Comet showers and the steady-state infall of comets from the Oort Cloud. *Astron. J.* 86, 1730–1740.
- Kenyon, S.J., Bromley, B.C., 2002. Collisional cascades in planetesimal disks. I. Stellar flybys. *Astron. J.* 123, 1757–1775.
- Kerr, R.H., 1961. Perturbations of cometary orbits. In: *Proc. Fourth Berkeley Symposium on Mathematical Statistics and Probability*, vol. 3. Univ. of California Press, Berkeley, p. 87.
- Kinoshita, H., Nakai, H., 1999. Analytical solution of the Kozai resonance and its application. *Celest. Mech. Dynam. Astron.* 75, 125–147.
- Kobayashi, H., Ida, S., 2001. The effects of a stellar encounter on a planetesimal disk. *Icarus* 153, 416–429.
- Kozai, Y., 1962. Secular perturbations of asteroids with high inclination and eccentricity. *Astron. J.* 67, 591–598.
- Kroupa, P., 2000. Constraints on stellar-dynamical models of the Orion nebula cluster. *New Astron.* 4, 615–624.
- Kroupa, P., Tout, C.A., Gilmore, G., 1993. The distribution of low-mass stars in the galactic disk. *Mon. Not. R. Astron. Soc.* 262, 545–587.
- Kroupa, P., Aarseth, S., Hurley, J., 2001. The formation of a bound star cluster: From the Orion nebula cluster to the Pleiades. *Mon. Not. R. Astron. Soc.* 321, 699–712.
- Lada, C.J., Lada, E.A., 2003. Embedded clusters in molecular clouds. *Annu. Rev. Astron. Astrophys.* 41, 57–115.
- Lada, C.J., Margulis, M., Dearborn, D., 1984. The formation and early dynamical evolution of bound stellar systems. *Astrophys. J.* 285, 141–152.
- Levison, H.F., Duncan, M.J., 1994. The long-term dynamical behavior of short-period comets. *Icarus* 108, 18–36.
- Levison, H.F., Morbidelli, A., Dones, L., 2004. Sculpting the Kuiper Belt by a stellar encounter: Constraints from the Oort Cloud and scattered disk. *Astron. J.* 128, 2553–2563.
- Morbidelli, A., Levison, H.F., 2004. Scenarios for the origin of the orbits of the trans-neptunian objects 2000 CR₁₀₅ and 2003 VB₁₂ (Sedna). *Astron. J.* 128, 2564–2576.
- Murray, C.D., Dermott, S.F., 1999. *Solar System Dynamics*. Cambridge Univ. Press, Cambridge, UK.
- Oort, J.H., 1950. The structure of the cloud of comets surrounding the Solar System and a hypothesis concerning its origin. *Bull. Astron. Inst. Neth.* 11, 91–110.
- Oort, J.H., Spitzer, L., 1955. Acceleration of interstellar clouds by O-type stars. *Astrophys. J.* 121, 6–23.
- Press, W.H., Teukolsky, S.A., Vetterling, W.T., Flannery, B.P., 1992. *Numerical Recipes in FORTRAN: The Art of Scientific Computing*, second ed. Cambridge Univ. Press, Cambridge, UK.
- Thommes, E.W., Duncan, M.J., Levison, H.F., 1999. The formation of Uranus and Neptune in the Jupiter–Saturn region of the Solar System. *Nature* 402, 635–638.
- Tsiganis, K., Gomes, R., Morbidelli, A., Levison, H.F., 2005. Origin of the orbital architecture of the giant planets in the Solar System. *Nature* 435, 459–461.
- Wisdom, J., Holman, M., 1991. Symplectic maps for the *n*-body problem. *Astron. J.* 102, 1528–1538.